Quarterly Report for

April 1997 - June 1997

Stanford Geothermal Program

DE-FG07-95ID13370

Table of Contents

1 AN EXPERIMENTAL STUDY OF BOILING IN POROUS MEDIA

This research project is being conducted by Dr. Cengiz Satik and Huda Nassori. The objective of this study is to improve our understanding of the process of boiling in porous media by using both experimental and numerical methods.

1.1 SUMMARY

The objective of this work is to improve the fundamental understanding of the process of boiling in porous media. The ultimate goal is to understand the origin of the two important but currently unknown functions of relative permeability and capillary pressure functions. During the previous quarter, a vertical experiment using a Berea sandstone core sample was initiated upon the completion of improvements and modifications to the apparatus. The experiment has been in progress for about 19 days in the vertical mode. The preliminary results of this experiment will be discussed.

1.2 INTRODUCTION

The process of boiling in porous media is of significance in geothermal systems as well as in many other applications such as porous heat pipes, drying and nuclear waste disposal. Despite its importance in these applications, the fundamentals of this process are poorly understood. Most of the problems arise from the lack of the understanding of the mechanics and dynamics of this complex process.

A look at the previous literature shows that many attempts have been made in both experimental and theoretical directions to investigate and to describe the process of boiling in porous media (Satik, 1994). Most previous studies have used continuum formulations which extended Darcy's law to multiphase flow with relative permeability and capillary pressure functions derived from isothermal gas-liquid displacement processes. These processes have major differences to boiling displacement which involves additional phenomena such as heat transfer, nucleation and phase change. Moreover, the continuum approaches are also limited by the assumption of capillary control at the pore level (low Capillary and Bond numbers). Due to these restrictions and uncertainties, it is unclear whether the relative permeability and capillary pressure functions currently used for modeling the process of boiling in porous media are appropriate. At the same time, fundamental studies focusing at the microscopic pore scale have been very limited. In a recent study by Satik and Yortsos (1996), numerical and experimental pore networks were used to model boiling in porous media at a microscopic scale. Satik and Yortsos (1996) developed a numerical pore network model for boiling in a horizontal, two-dimensional porous medium and conducted visualization experiments by using glass micromodels. Although progress was made, their model was developed only for a single bubble growth problem in a horizontal porous medium, ignoring the effects of gravity. Therefore, further work is still needed to improve the understanding and to resolve the issues raised by the continuum formulations (see Satik, 1994, for

details) and eventually to obtain appropriate forms of the relative permeability and capillary pressure functions.

In this work, we are conducting boiling experiments with real core samples such as from Berea sandstone. Using an X-ray computer tomography (CT) scanner, we area able to visualize the process and determine the three-dimensional fluid distributions within the core while the experiment is in progress. By using thermocouples, pressure transducers and heat flux sensors under the control of a data-acquisition system, we can obtaine temperature, pressure and heat flux values along a core, respectively. The comparison of the experimental data with the results of numerical simulation will give us an opportunity to check the numerical results.

1.3 RESULTS

A vertical boiling experiment was initiated after completing the modifications suggested by the previous experiment reported in the last quarterly report. This experiment will consist of both heating (increasing heat flux) and cooling (decreasing heat flux) stages. Following the cooling stage the core will be positioned horizontally and another heating-cooling cycle will be conducted. Eventually, the results of horizontal and vertical boiling experiments will be analyzed and compared to improve the fundamental understanding of the boiling in porous media The experiment is currently in progress in the vertical mode. The results of the first 19 days of this experiment are discussed in this section.

A schematic of the experimental apparatus and procedure were given in the previous quarterly report. Briefly, the apparatus consists of a core holder, a data acquisition system, a vacuum pump, a liquid pump and a balance to measure the outflow and inflow. Eleven pressure taps and thermocouples are placed along the core length to measure pressures and temperatures, respectively. A heater and a heat flux sensor are placed at the inlet end of the core holder. In addition, eleven heat flux sensors are placed along the core to measure heat losses. In order to obtain more information towards the heater, the first eight pressure taps, thermocouples and heat flux sensors from the heating side of the core are located at every 3 cm from the heater while the remaining three are 6 cm apart from each other. During an experiment, the core holder is placed inside the high resolution X-ray CT equipment to obtain *in-situ* saturation profiles along the core (Satik, 1997).

The core used in this experiment is a Berea sandstone core with a permeability of about 600 md. Before the experiment, the core was preheated at 450^{o}C to deactivate clays. After assembling the core holder and auxiliary, the core was mounted into the X-ray CT scanner and kept under vacuum conditions for several hours to remove the air inside the pore space. After being scanned to obtain dry CT values, the core was saturated completely with deaerated water. The core was then scanned again to obtain wet CT values. Using these two sets of CT values, the porosity distribution in the core was

obtained by using the method described in Satik (1997). Figure 1.1 shows a three-dimensional porosity image of the core. The average porosity of the core was found to be around 21%.

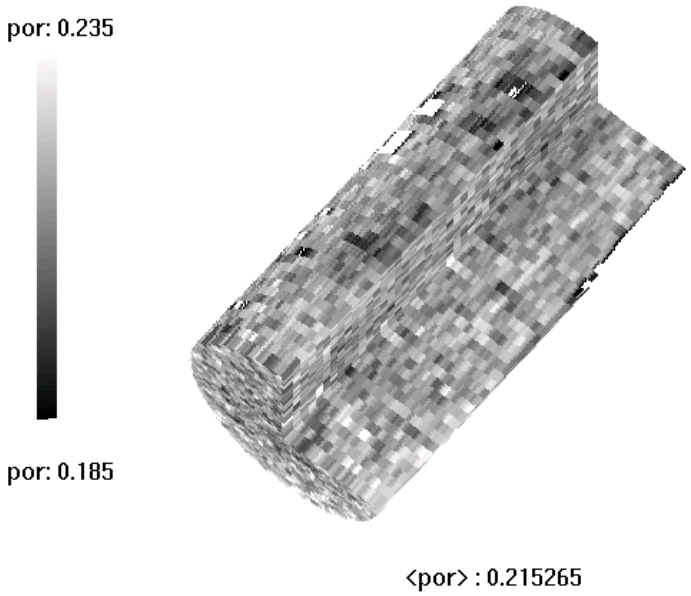

Figure 1.1: Three-dimensional porosity distribution of the core used in the experiment.

Figure 1.2 shows the history of the heater power setting and the corresponding heat flux reading. During the initial warming-up stage the power to the heater was increased slowly to avoid thermal shock to the epoxy core holder. The core was scanned several times to check any possible gas (air) formation inside the pore space at temperatures lower than the actual boiling temperature. Using these X-ray CT values, three-dimensional porosity profiles were calculated. Figure 1.3 shows seven average porosity profiles obtained by averaging the porosity distributions over the cross-sectional area. As shown in Figure 1.3, except the curve labeled “wet6” all of the other curves are coincident with each other. The slight decrease observed in porosity towards the heater may be attributed to the density change as temperature increases. The significant deviation observed on the curve wet6 (as much as 3%) indicates the presence of a gas phase, which is identified as steam by examining the temperature and pressure profiles obtained at the same time. This result confirmed that the air both inside the pore space and in the water used to saturate it had been successfully removed. After the onset of the first steam formation inside the pore space, the heater power setting value was kept at 45% for 20 hours Following this, the power was set to 50% for 70 hours, 55% for 180 hours and finally to 60% for 160 hours. These long waiting times allowed the system sufficient time to reach steady state conditions. During the process of increasing heater power, the core was scanned to obtain CT values and three-dimensional steam saturations were calculated by using the method described in Satik (1997). Figure 1.4 shows three-dimensional steam saturation images at four heater power settings (45, 50, 55 and 60%). At each stage, steady state conditions

were confirmed by examining the temperature, pressure, liquid mass produced from the core and heat flux readings (flattening portions of the curves in Figure 1.5).

At the end of each power setting steady state steam saturations were obtained. Figure 1.6 shows 17 average steam saturation profiles obtained during this experiment. The expected results were obtained. A two-phase zone followed by a single-phase liquid zone (curve sst0) was obtained at lower heat fluxes while a two-phase zone between single-phase steam and liquid zones was obtained at higher heat fluxes, as shown in the saturation profiles given in Figure 1.6. These results are also apparent from the temperature profiles shown in Figure1.8. The first two profiles (at time = 56.67 and 121 hours) have the characteristics of a two phase region (almost flat temperature profile) followed by a single-phase liquid zone while the last profile(time = 450.17) indicates a two-phase region (almost flat profile) between single phase steam and water regions. Once a dry steam zone forms the temperature gradient over this zone becomes large due to the relatively small steam thermal conductivity.

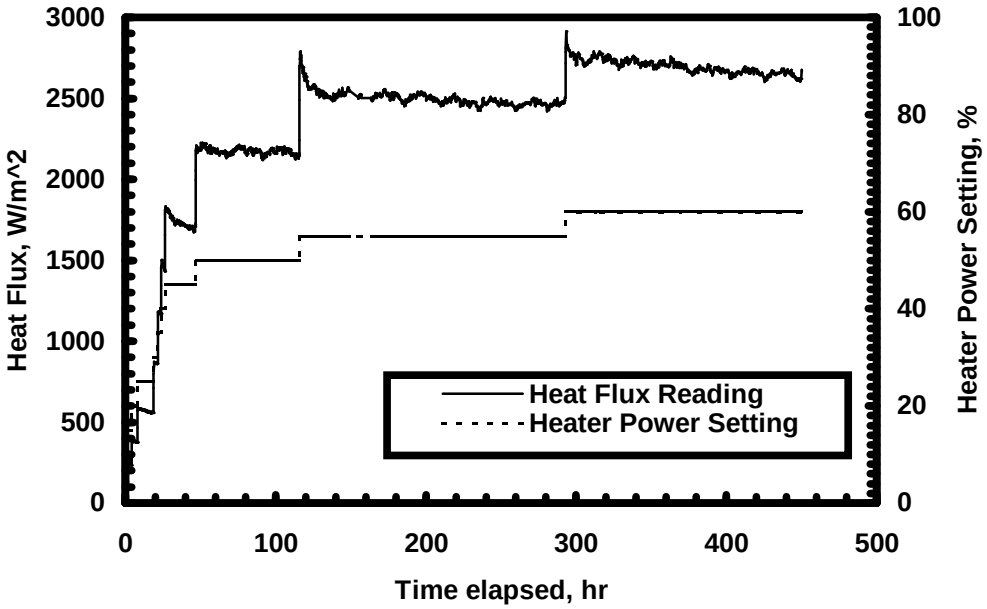

Figure 1.2: Heater power settings and corresponding heat flux values obtained from the heat flux sensor.

1.3 FUTURE WORK

During the next quarter, the vertical boiling experiment will be completed and an attempt will be made to use the same core for the horizontal boiling experiment. Also a numerical simulator will be used to match the experimental data, as described in Section 3 of this report.

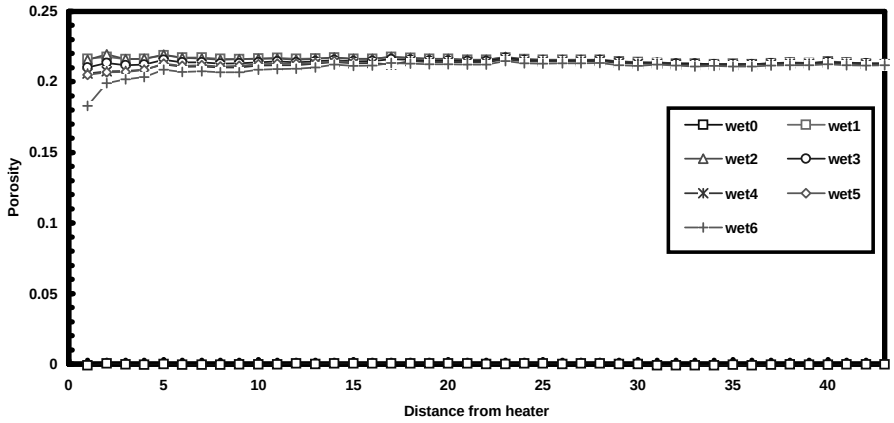

Figure 1.3: Average porosity profiles during the initial warm-up stage.

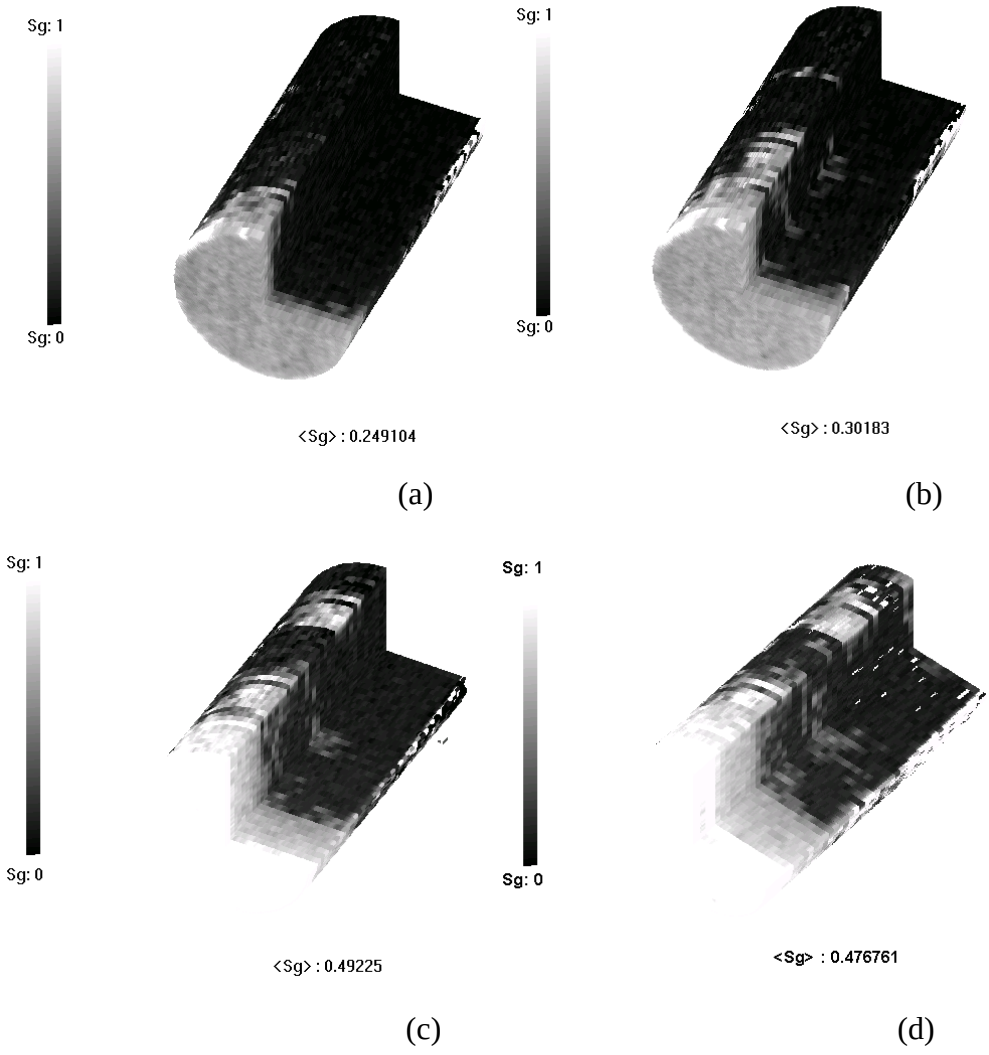

Figure 1.4: Three-dimensional steam saturations obtained at four different heater power settings: (a) 45%, (b) 50%, (c) 55% and (d) 60%.

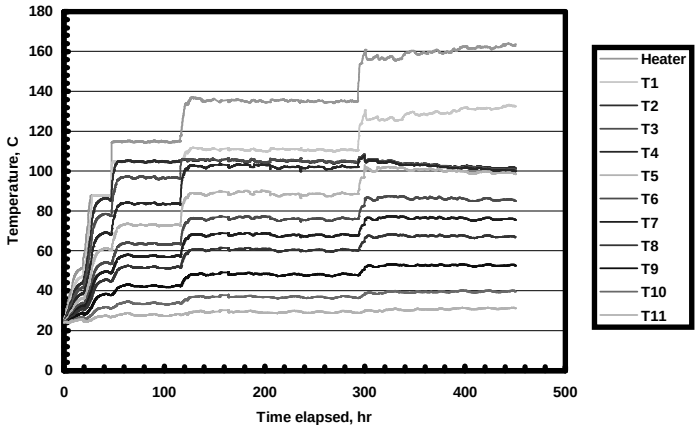

(a)

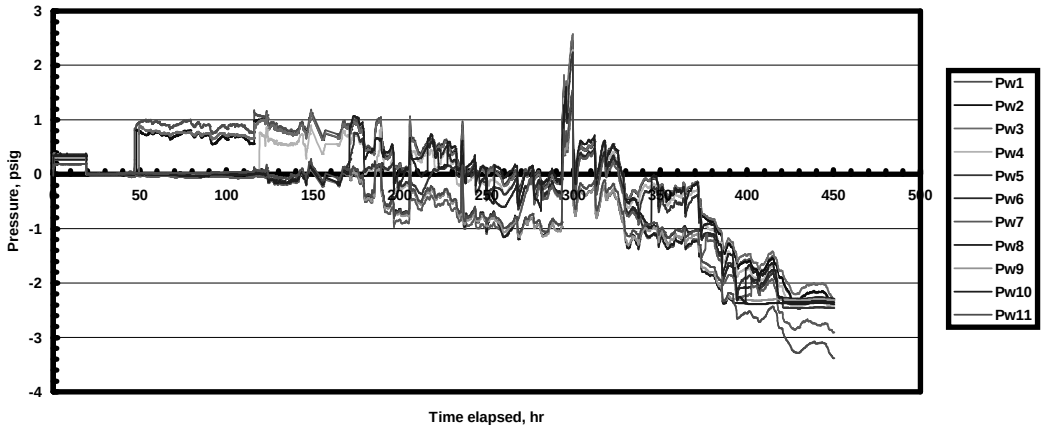

(b)

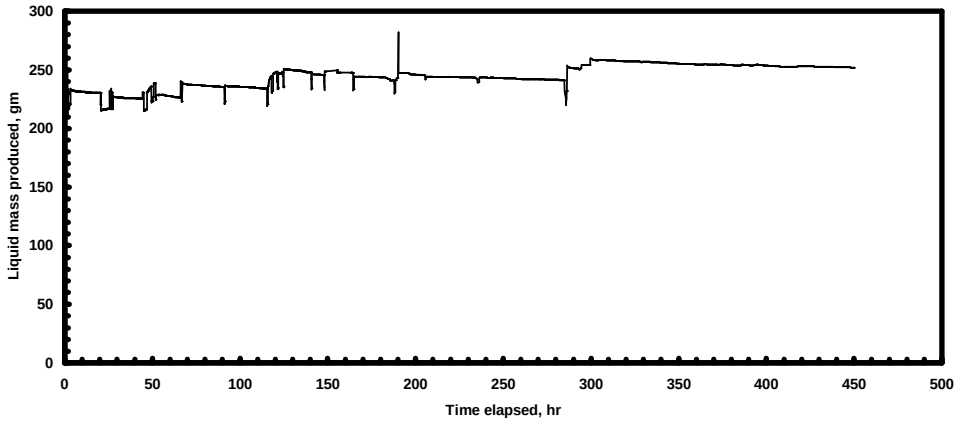

(c)

Figure 1.5: Histories of (a) wall temperatures and heater temperature, (b) pressures and (c)liquid mass produced during the vertical boiling experiment.

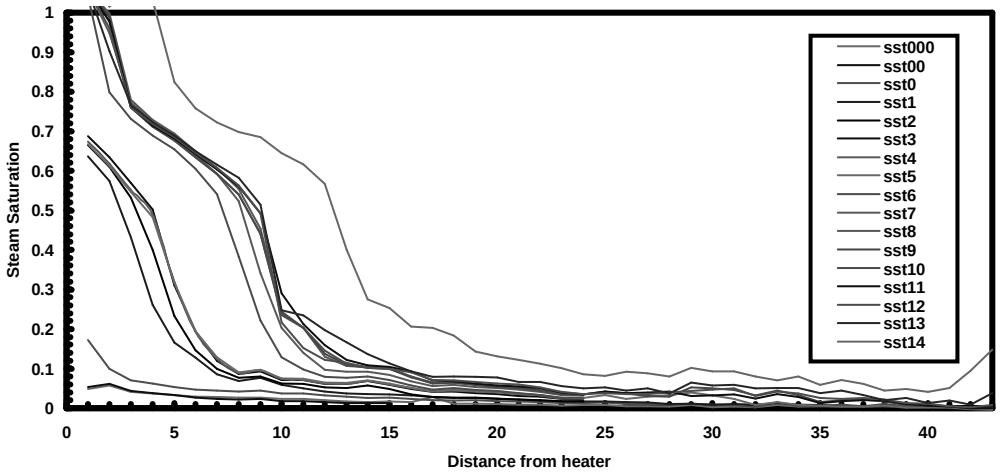

Figure 1.6: Steam saturation profiles obtained during the vertical boiling experiment.

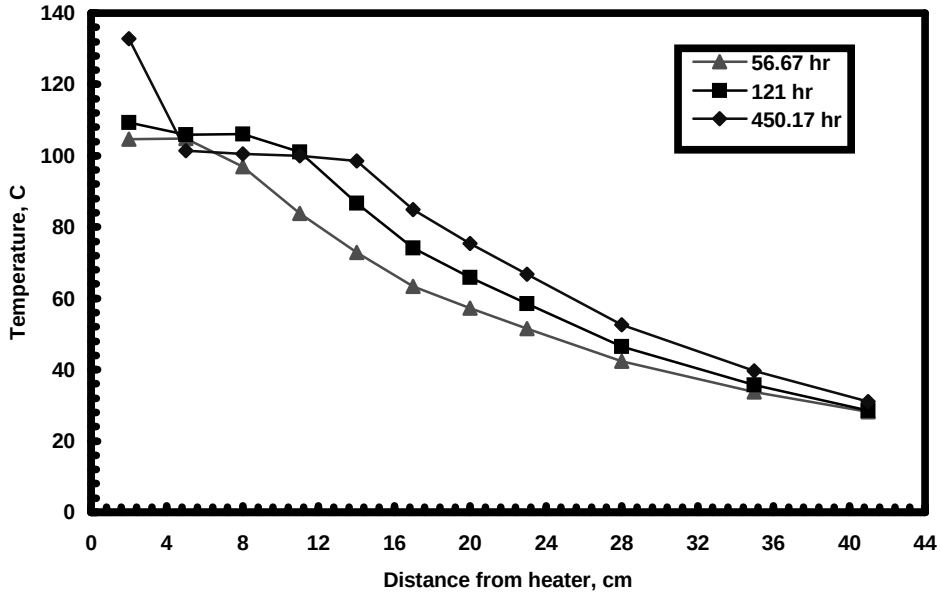

Figure 1.7: Steady state wall temperatures obtained at three power values during the vertical boiling experiment.

2 MEASUREMENTS OF STEAM-WATER RELATIVE PERMEABILITY

This project is being conducted by Research Assistant Raul Tovar, Dr. Cengiz Satik and Professor Roland Horne. The aim of this project is to measure relative permeability relations for steam and water flowing simultaneously in a porous medium.

2.1 SUMMARY

Experimental efforts continued towards obtaining relative permeability for steam-water flow in a homogeneous porous medium under adiabatic steady-state conditions. The porous media used in the experiments were Berea sandstone core samples. Porosity and saturation distribution were measured using a high resolution X-ray computer tomography (CT) scanner. Steam fractional flow, crucial in evaluating relative permeabilities, was monitored using a computer data acquisition system for measuring temperatures, pressures and heat fluxes. In particular, two approaches were investigated: (1) the simultaneous injection of steam and water and (2) the injection of water while it goes through a phase change. Both methods required assumptions with respect to two-phase flow and heat transfer, which lead to uncertainty in the results. Nonetheless, injecting through a single line greatly simplified the experiments.

2.2 EXPERIMENTAL APPARATUS AND PROCEDURE

The experimental apparatus consisted of a CT scanner (Figure 2.1) and a core holder (Figure 2.2). The scanner was an X-ray computer tomography device with a resolution of 0.5 millimeter. The scanner measured porosity and in-situ saturation in the core while the experiment was in progress. The scans were obtained at every centimeter along the core when steady-state conditions were reached. The principles of the use of X ray CT are described in Johns et al. (1993) and a brief summary is given also by Satik et al. (1995).

The samples used were homogeneous Berea sandstone cores 43 cm in length and 5 cm in diameter. Before the experiment, the core sample was heated to 450°C for about twelve hours to deactivate clays and to get rid of any trapped water. The core was then covered with high temperature epoxy (Duralco-4461 manufactured by Cotronics). Eight 1/16" ID Swagelok pressure ports were fixed with epoxy at five centimeter intervals. Injection and production ports (1/8" ID) were also fixed with epoxy at the ends of the core. Detailed explanations of the epoxy preparation, application to the core and difficulties encounter were discussed by Ambusso (1996).

Eight Rdf brand micro foil T-type thermocouples/heat flux sensors were installed at the same axial locations as the pressure ports to measure temperature and radial heat losses along the core. The core was tested for leaks before being covered with an insulation

material made of ceramic blanket. In addition, nine pressure ports and nine J-type thermocouples were installed in the injection and production lines.

(a) ***(b)***

Figure 2.1: Pictures of (a) the core holder and X-ray CT scanner couch and (b) the CT scanner controls used in the experiments.

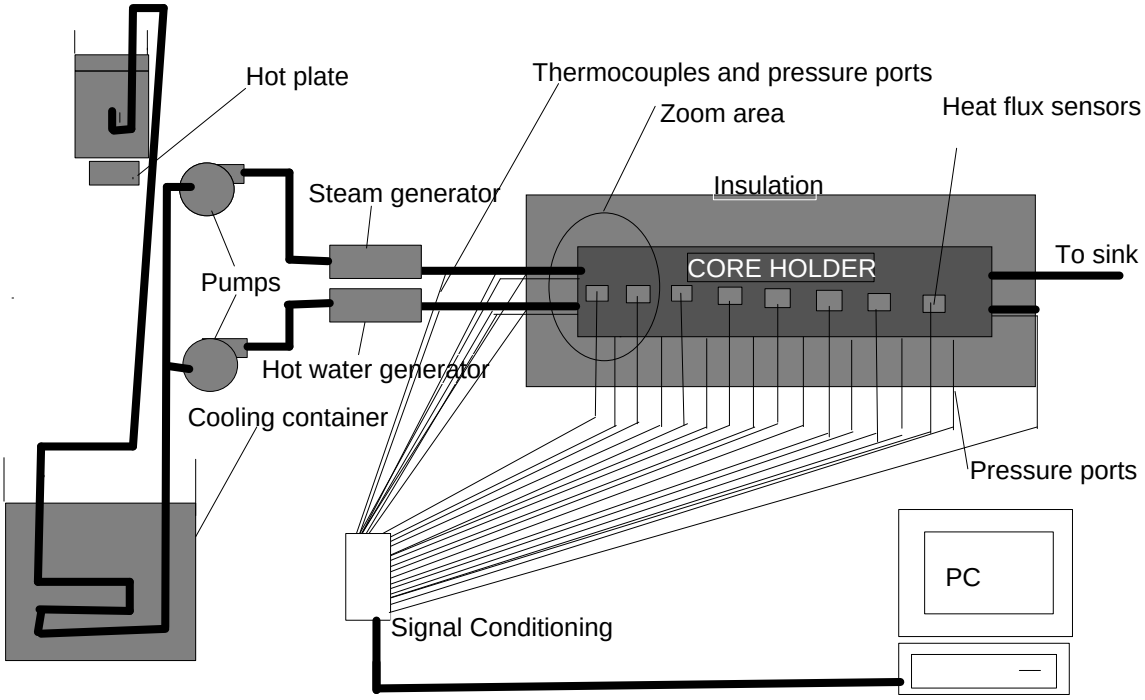

Figure 2.2: Experimental apparatus for simultaneous injection experiments to obtain steam-water relative permeabilities. and thermocouples

The pressure transducers used were Celesco model KP-15 and Custom Electronic Systems, Inc. model 238-FP-10psi-5v-3w. The piping used for the experiments was 1/8" and 1/16" ID Teflon tubing with stainless steel Swagelok fittings. All lines between the furnaces and the core holder were covered with ceramic blanket to avoid heat losses. Two furnaces were used to generate steam and hot water. The furnaces, steam and hot water generators, had maximum capacities of 1.9 KVA and 1.7 KVA respectively. Two power controllers were used to control the energy supplied by each of the two furnaces. The fluids were injected by two Dynamax SD-200 solvent delivery pumps made by Rainin.

The proportional voltage signals from the heat flux sensors, thermocouples and pressure transducers were first conditioned and then collected in a personal computer by a data acquisition system through an AT-MIO-16DE-10 data acquisition card. The data was then analyzed using "LabVIEW", version 4.0, a graphical programming software by National Instruments. "LabVIEW" used control panels as interactive interfaces for supplying inputs to and observing outputs from the experimental apparatus. The program used a code diagram that contained icons representing input/output operations, computational functions, and analysis functions to organize the program source code. The source code was a modification of a "Temperature Monitor" example program included in the software package. The program monitored temperatures, heat fluxes and pressures on a four chart panel as well as on a panel similar to Figure 2.2, shown in Figure 2.3. The program could save the data in spreadsheet form as often as needed, allowing further data processing and analysis. A steam table calculation was used to signal and alert if saturation conditions were reached, which was crucial to this experiment. Heat flux measurements were made using heat sensors that produced an analog output DC voltage of ±10mV. The relationship between voltage and heat flux was directly proportional at constant temperature. For varying temperatures a correction factor chart was provided for each heat sensor by the manufacturer. This chart was interpolated directly within the software code to output real time heat flux in watts per square meter. In addition, the software calculated real time absolute permeability, the flowing fraction of steam and steam-water relative permeabilities.

The signal conditioning hardware consisted of an SCXI-1000 chassis, two SCXI- 1100 multiplexer amplifiers and two SCXI-1300 terminal blocks, all manufactured by National Instruments.

Initially the insulated core holder was secured firmly on the CT scanner couch to ensure scanning of the same locations throughout the experiment. Although heat losses were measured, it was important to insulate the core holder well to obtain sufficiently flat saturation and temperature profiles. Using the vacuum pump, most of the air inside the pore space was evacuated. Under vacuum conditions the core was then scanned along its length to obtain dry CT scan numbers (CT_{dry}).

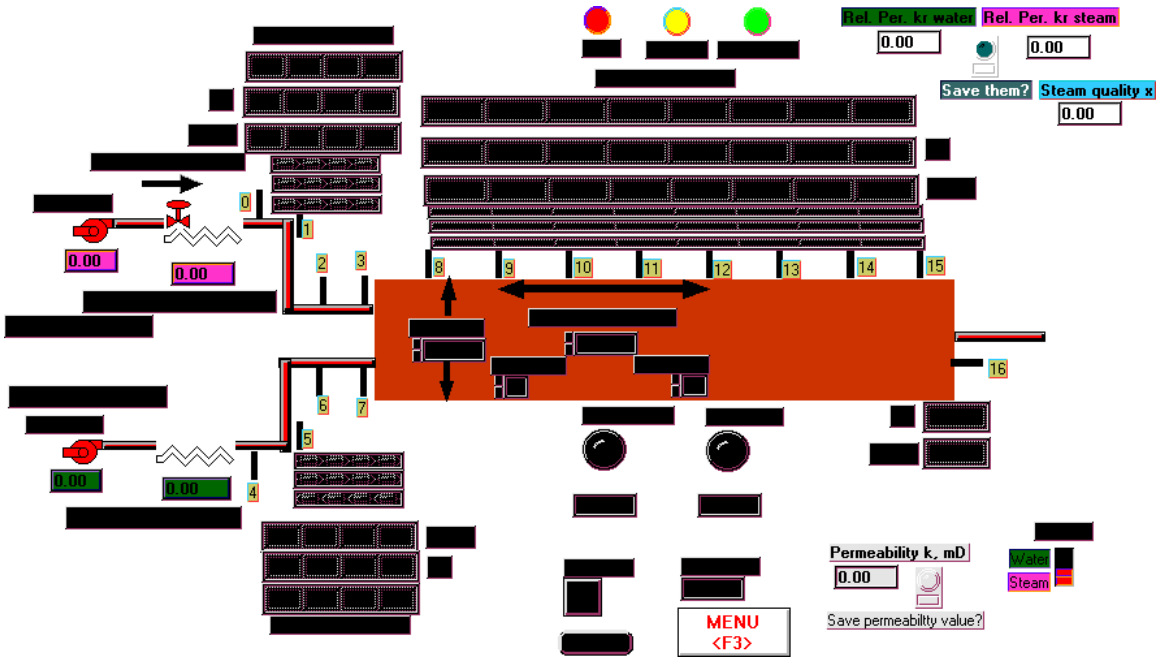

Figure 2.3: "LabVIEW" control panel.

Deionized water was boiled on a hot plate to remove air initially dissolved in the water that could give erroneous saturation readings (Ambusso, 1996). The water was then passed through a cooling container as shown in Figure 2.2. Cooling the water was necessary in order to avoid damage to the pump. Cold water at room temperature was injected to the core through the steam generator line. The flow rate depended on the particular core sample inlet pressure. In general, the set ranges varied from 1cc/min to 10cc/min. Once breakthrough was achieved water was allowed to flow for at least a couple of pore volumes to fully saturate the core. Scans were then made to obtain wet CT scan numbers (CT_{wet}) at the same locations as the dry scan had been made. The next step was to prime the lines connecting the pressure ports to the pressure transducers. The steam generator power controller was turned on. Water temperature was increased in steady-state steps. With the pressure transducers primed, absolute permeability was monitored versus temperature. At steady state, once the temperature was at a step close to saturated conditions scans were taken to obtain hot wet CT scan numbers (CT_{hwet}).

Two approaches were studied to obtain relative permeability versus saturation. The first was the simultaneous injection of steam and water to the core using two independent lines. The second was the injection of water through a single line while it underwent a phase change in the furnace. As emphasized later, the ability to obtain the fractional flow of steam (or water) is crucial in the evaluation of relative permeabilities as the rest of the variables, with the exception of absolute permeability, can be measured directly or can be interpolated from steam tables with the knowledge of fluid temperature. These methods were conceived from the literature described by Ambusso (1996), Piquemal (1994), and

Sanchez and Schechter (1987). Independently of the method used, once steady-state was distinguished by constant temperatures and pressures over a period of time, the core was scanned to obtain the corresponding saturated CT scan numbers (CT_{sat}).

2.3 CALCULATIONS

Porosity

An interpretation software (FPviewer) was used to evaluate the porosity and saturation distributions from the CT numbers. To calculate porosity the following expression was used (Satik et al., 1995):

$$\phi = \frac{CT_{wet} - CT_{dry}}{CT_{water} - CT_{air}} \tag{2.1}$$

where CT_{water} and CT_{air} are predetermined calibration CT numbers for water and air, respectively.

The average porosity distribution on most of the core samples was about 20%. Each slice was calculated using Equation (2.1). The porosity distribution along the length of two core samples is plotted in Figure 2.4. The uniform distribution is consistent with the assumption that the core samples are homogeneous.

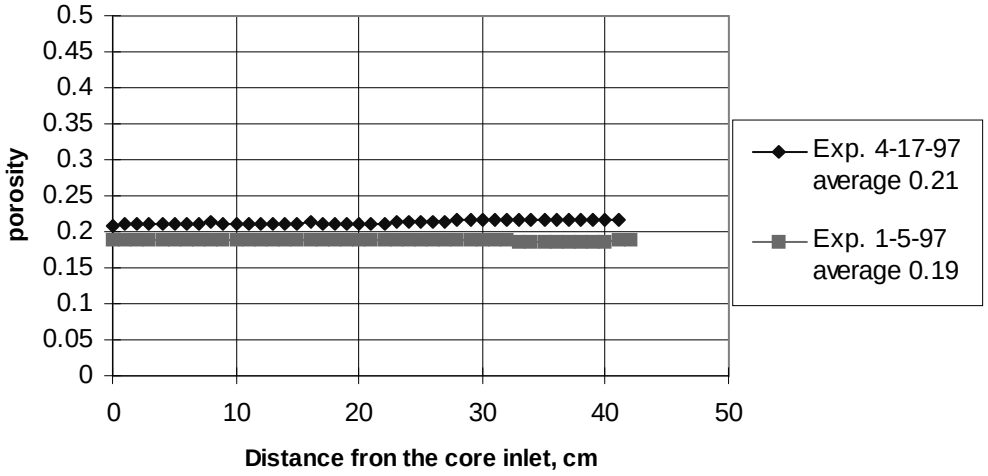

Figure 2.4: Porosity distributions for two Berea sandstone core samples.

Saturation

Analogous to Equation (2.1) the steam saturation can be calculated as follows:

$$S_s = \frac{CT_{wet} - CT_{sat}}{CT_{wet} - CT_{dry}} \tag{2.2}$$

$$S_l = 1 - S_s \tag{2.3}$$

where S_l and S_s denote liquid water and steam saturations, respectively.

Figure 2.5 illustrates the steam saturation profile of a core sample taken at a time when the temperature and pressure distributions were as shown in Figure 2.6 and Figure 2.7, respectively. The temperature and pressure measurements clearly indicate that no steam can exist along the core. This implies that the values obtained in Figure 2.5 might be attributed to the variation of liquid density with temperature. Therefore to obtain correct the steam saturation distributions Equation (2.2) could be modified as follows:

$$S_s = \frac{CT_{hwet} - CT_{sat}}{CT_{hwet} - CT_{dry}} \tag{2.4}$$

where CT_{hwet} is the scan number taken near saturated conditions and was previously defined as the hot wet scan number.

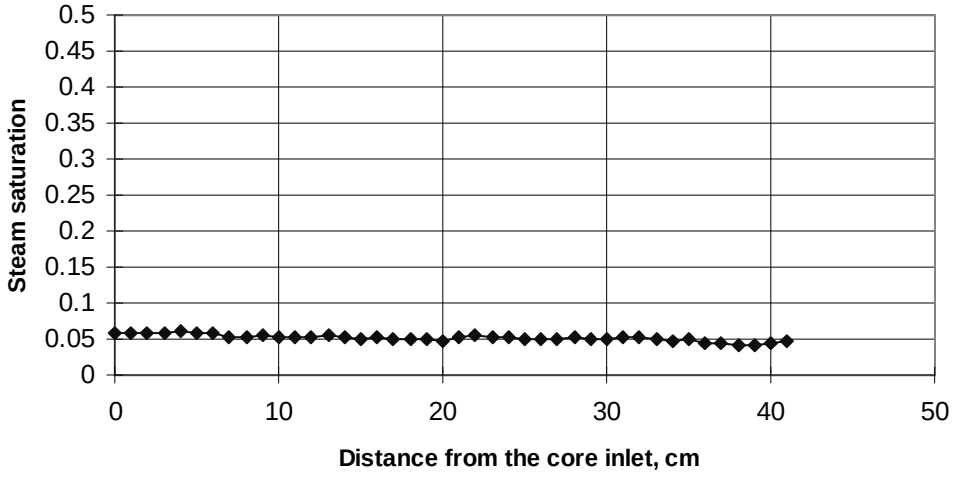

Figure 2.5: Steam saturation distribution along the length of the core sample from experiment "Exp. 4-4-97".

Figure 2.8 shows CT images at the inlet of the core obtained using Equations (2.2) and (2.4). Figure 2.9 illustrates the steam saturation profile difference along the core using both equations. This figure demonstrates the error that can be incurred by using cold wet scans. The wet scan must be as close as possible to saturated conditions while being careful not to be in the two-phase zone.

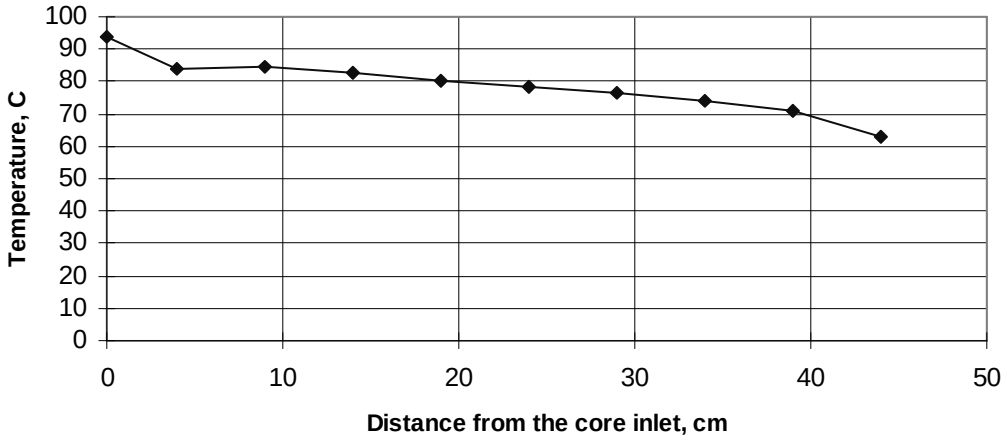

Figure 2.6: Temperature profile along the core sample from experiment "Exp. 4-4-97".

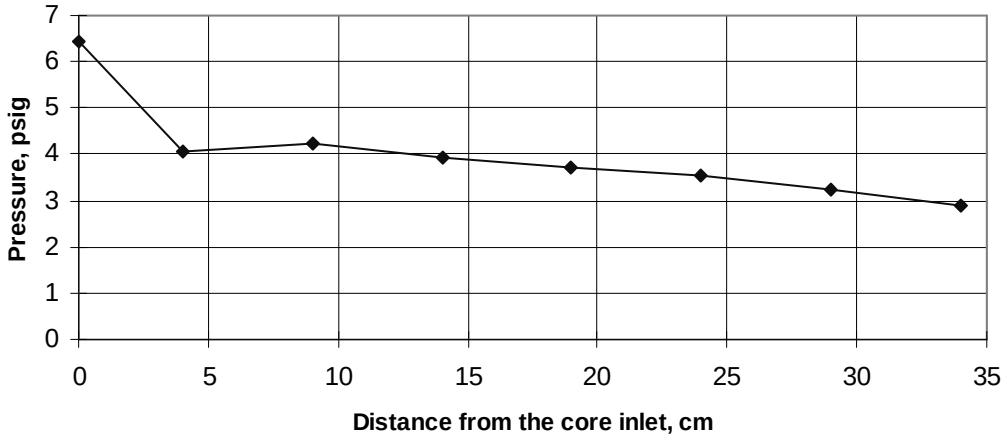

Figure 2.7: Pressure profile along the core sample from experiment "Exp. 4-4-97".

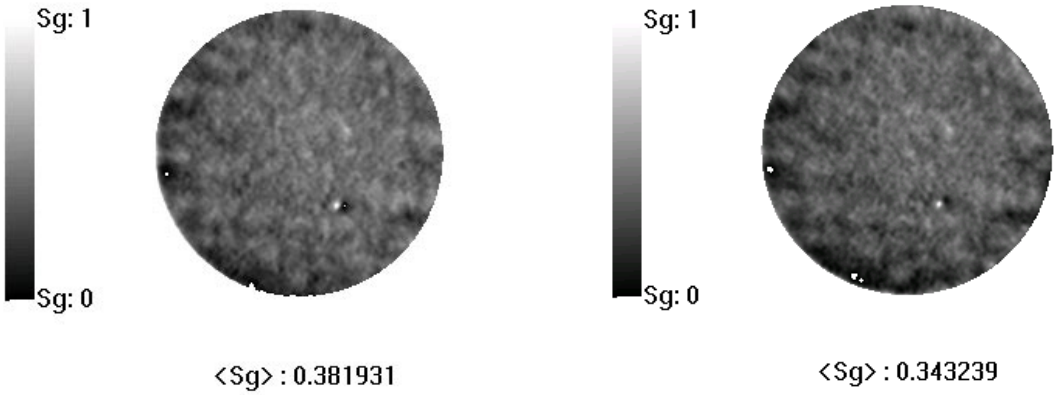

(a) (b)

Figure 2.8: Saturation distribution images at the core inlet obtained using (a) Equation (2.2) and (b) Equation (2.4).

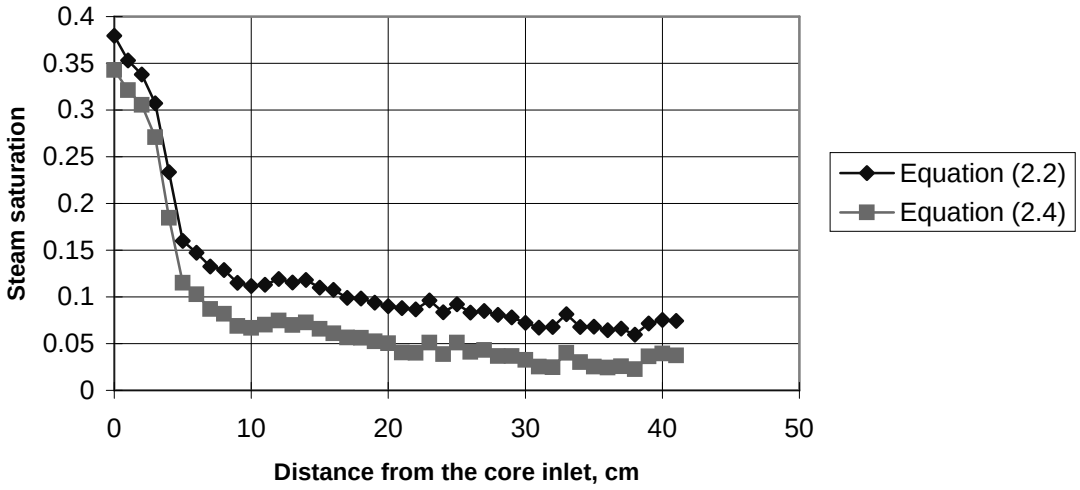

Figure 2.9: Comparison of two steam saturation profiles along a core sample.

Absolute permeability

Absolute permeability is evaluated using Darcy's law:

$$k = \frac{\mu q \Delta x}{A \Delta p} \tag{2.5}$$

where q is the flow. These parameters can be measured directly with the exception of viscosity. With the appropriate water property table, viscosity can be estimated from fluid temperature measurements.

Experimental results of absolute permeability as a function of temperature are illustrated in Figures 2.10 to 2.13. Figure 2.10 shows absolute permeability measured over a time interval of 250 minutes for the core sample of the experiment labeled "Exp. 12-29-96". Each curve represents measurements at a constant flow rate of 10 cc/min taken at different temperatures of 40^{o}C and 62^{o}C. These curves indicate no major variation in permeability as a function of temperature. Figure 2.11 shows absolute permeability for core sample of experiment "Exp. 1-5-97".

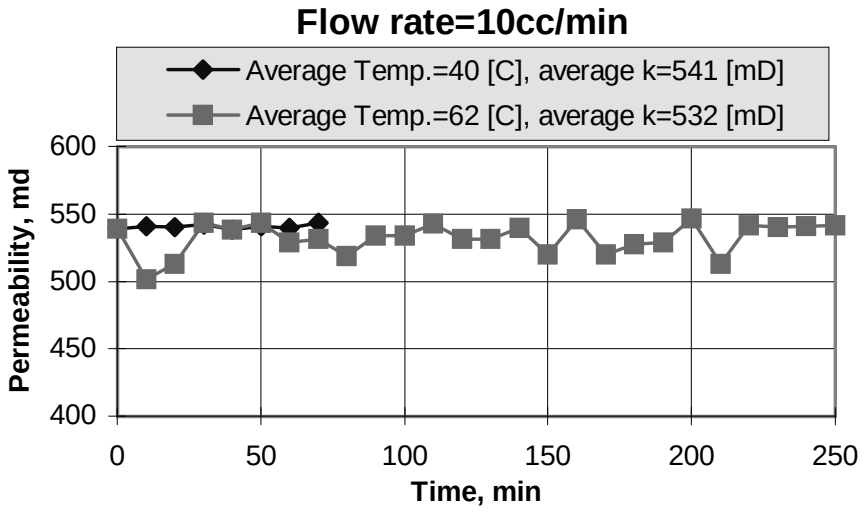

Figure 2.10: Comparison of permeability at two different temperatures for experiment "Exp. 12-29-96".

The first curve was measured while the water temperature was increased from 39^{o}C to 88^{o}C at 10cc/min in a period of 250 minutes, and shows only small permeability variation with temperature. The second curve was measured at a constant temperature of 22 ^{o}C and a flow rate of 5cc/min. in a period of 90 minutes. Both curves basically overlap implying a negligible flow rate dependence. Figure 2.12 and Figure 2.13 show measurements obtained while the water temperature was increased from 22 ^{o}C to 105 ^{o}C in about 20 hours. The low permeability values of about 900 md are attributed to the onset of two-phase flow whereas the values were obtained using Darcy's law for single phase flow. These results reveal once again no significant permeability change with respect to temperature.

The literature reports contradictory results on temperature dependence. Trimble and Menzie (1975) reported a permeability increase of 0.23md per °C. On the other hand, according to most of the papers reviewed by Chawathe and Sharma (1991), absolute permeability decreases with increasing temperatures. In addition, Ambusso (1996) reported absolute permeability variations with different flow rates. In general, Figures 2.10 to 2.13 indicated only small absolute permeability variations with temperature and flow rate. We believe that such small variations can be attributed to the precision of the pressure transducers and are within experimental error. Small permeability measurements of the order reported by Trimble and Menzie (1975) could not be measured with our experimental apparatus. However for the purpose of this experiment we conclude that permeability variation with temperature and flow rate is negligible.

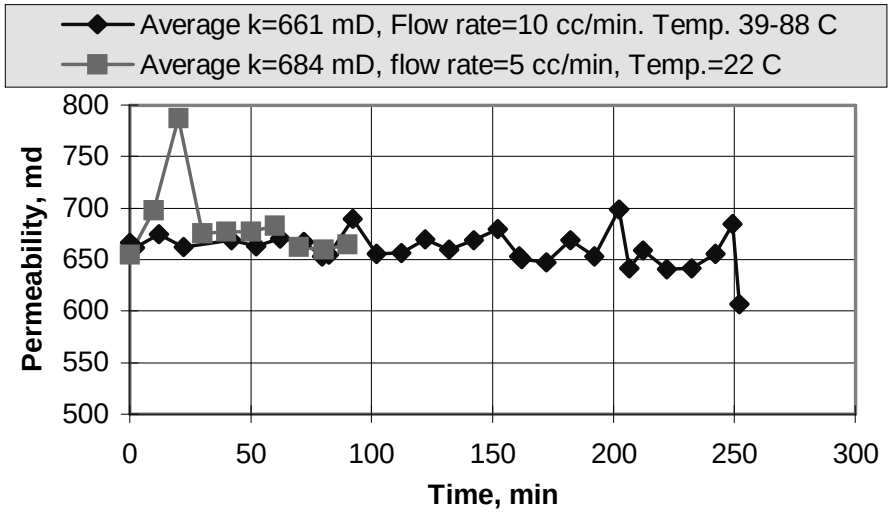

Figure 2.11: Absolute permeability variation with flow rate and temperature for experiment "Exp. 1-5-97".

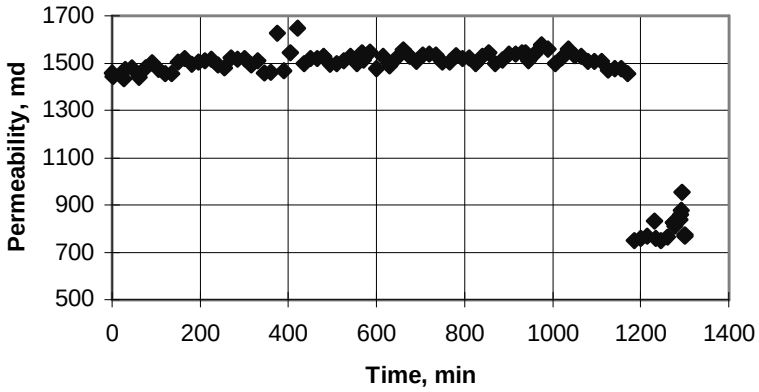

Figure 2.12: Permeability variation as temperature was increased to 105°C in a period of twenty hours from experiment "Exp. 4-17-97".

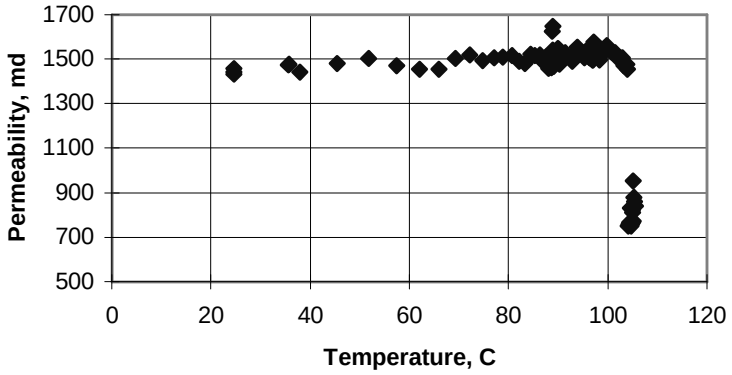

Figure 2.13: Absolute permeability variation with respect to temperature from experiment "Exp. 4-17-97".

2.4 RESULTS

METHOD I: Simultaneous steam and water injection

Mass flowing fractions can be calculated by applying the following mass and energy conservation equations:

$$m_t = m_s + m_l \tag{2.6}$$

$$m_s h_s + m_l h_l = m_t h_t + Q \tag{2.7}$$

where m and h denote mass flow rate and enthalpy, respectively and the subscript t refers to total, s to the steam phase and l to the liquid phase. Q is the total heat lost upstream of the point being considered.

To apply these equations to the control volume shown in Figure 2.14, at point 1, superheated steam was injected at a know rate m_1, pressure p_1 and temperature T_1. At the same time liquid hot water was injected at point 2 at a known rate m_2, pressure p_2 and temperature T_2. Using a superheated steam table we can interpolate T_1 and p_1 to obtain h_{1s}. Similarly, from a saturated steam table we can approximate h_2 from T_2 by using h_{2l}, the enthalpy at the saturated liquid phase. At point 3, under saturated conditions, from a saturated steam table and using either p_3 or T_3 we can obtain h_{3l} and h_{3ls}, the liquid phase enthalpy and the latent heat of vaporization respectively. Q is obtained by using the measured radial heat flux sensor value Q":

$$Q = Q'' A_s \tag{2.8}$$

where A_s is the cylindrical surface area of the core from point 1 (or point 2) to point 3.

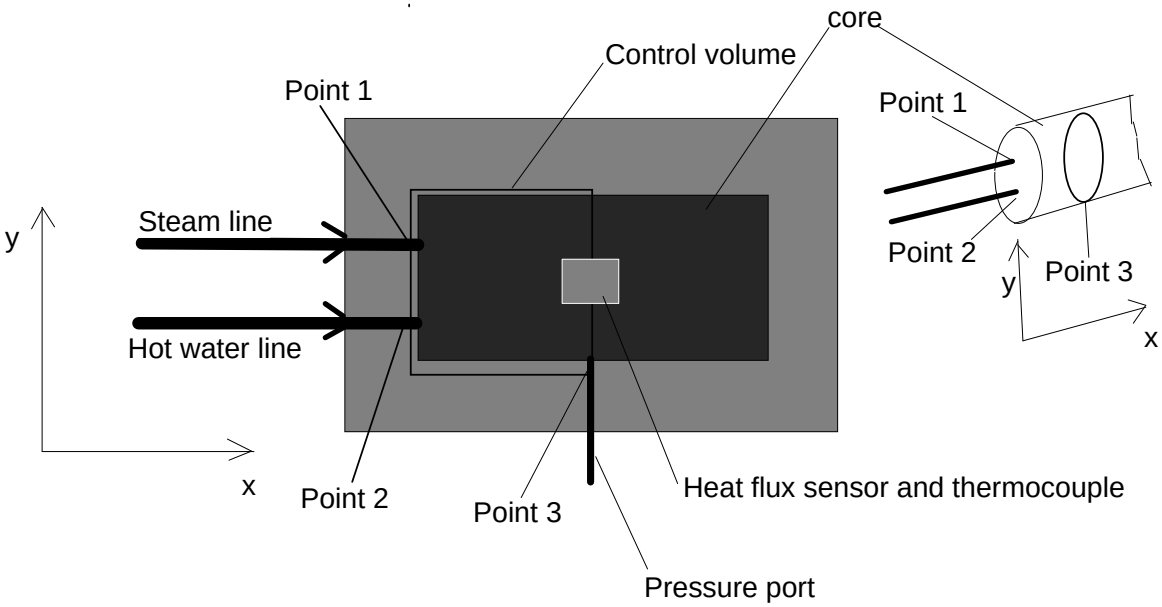

Figure 2.14: Control volume from Figure 10 zoom area.

Substituting in Equation (2.6):

$$m_3 = m_1 + m_2 \tag{2.9}$$

and Equation (2.7):

$$m_1 h_{1s} + m_2 h_{2l} = m_3 h_3 + Q'' A_s \tag{2.10}$$

where:

$$h_3 = h_{3l} + x h_{3ls} \tag{2.11}$$

Hence the steam flowing fraction x can be solved to be:

$$x = \frac{m_1 h_{1s} + m_2 h_{2l} - Q'' A_s}{m_3 h_{3ls}} - \frac{h_{3l}}{h_{3ls}} \tag{2.18}$$

Then the relative permeabilities to steam and water can be calculated for each phase in terms of the mass flow rates by Equations (2.14) and (2.15):

$$k_{rl} = -\frac{(1-x) m_t \mu_l \nu_l}{kA \frac{\Delta p}{\Delta x}} \tag{2.14}$$

$$k_{rs} = -\frac{x m_t \mu_s \nu_s}{kA \frac{\Delta p}{\Delta x}} \tag{2.15}$$

Figure 2.15 and Figure 2.16 show temperature and pressure results from experiment "Exp. 1-5-97". Figure 2.15 presents the temperature variation for the steam injection line, liquid water injection line and a point in the core four centimeters downstream of the injection lines.

The injection lines were heated until saturated conditions were reached. At this time heat was added only to the steam line with the hope it would reach superheated conditions. However no matter how much the power to the steam generator was raised it was not possible to confirm that superheated conditions were reached from temperature and pressure measurements. This is clearly illustrated in Figure 2.16 where all the measurement readings collapse to one point at saturated conditions. In Figure 2.15 this is shown by the overlapping of the temperature and pressure measurements. This difficulty was also encountered by Ambusso (1996) and a similar problem in the mixing of steam and water was discussed by Sanchez and Schechter (1987). Ambusso (1996) estimated the steam flowing fraction by extrapolating into the two-phase zone the single liquid phase slope of temperature (enthalpy) versus heat supplied. This implies that heat losses in the two-phasezone are equal to heat losses in the liquid single-phase zone. By making such assumptions, the experiment can be simplified as outlined in the next section.

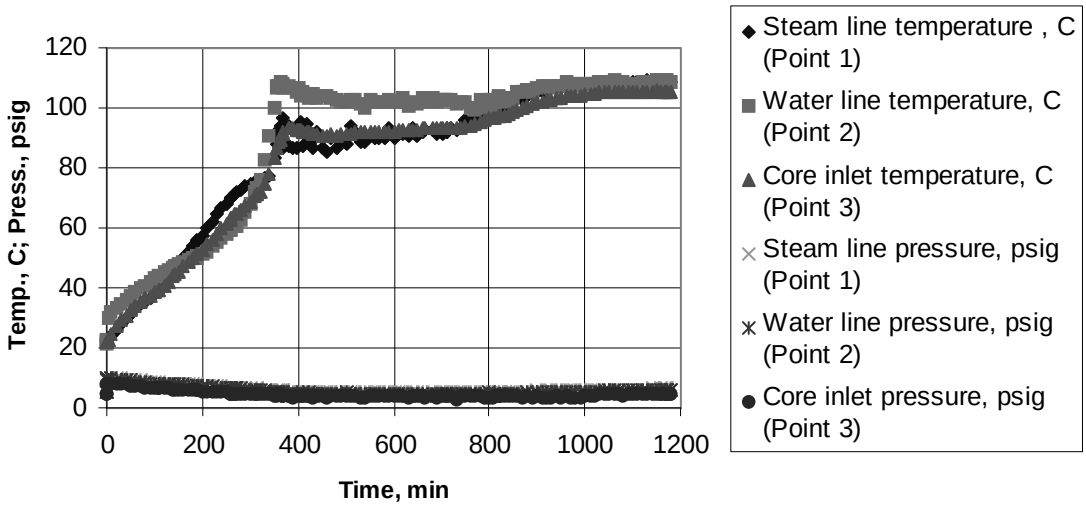

Figure 2.15: Temperatures and pressures from experiment "Exp. 1-5-97".

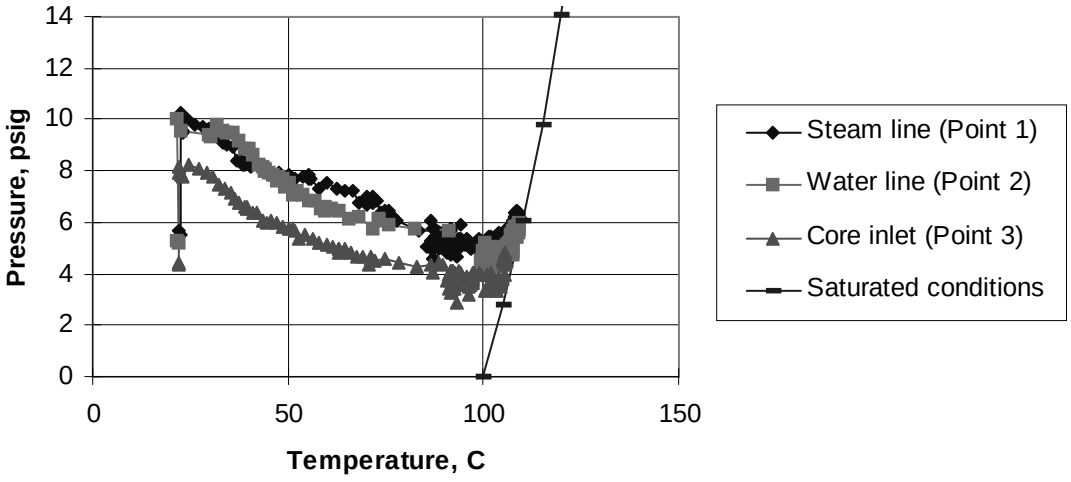

Figure 2.16: The collapse of data at saturated conditions.

<u>METHOD II: Single injection line</u>

In Method I, the experimental apparatus consisted of an injection unit with two furnaces to generate steam and hot water. However, uncertainty on the injection of superheated steam was a problem. Therefore the design was changed to a similar system with only a single injection unit as shown in Figure 2.17. The apparatus consisted of one power controller with a variac used to control the heat supplied by the steam generator.

During the experiment, the power of the steam generator was increased in steady state steps. That is, before the power was increased to the next step steady state conditions had to be reached. Initially the water was at subcooled conditions and was slowly brought up to the liquid saturation line. Then the power was raised in steps through the saturation zone until the steam saturation line was reached (Figure 2.18).

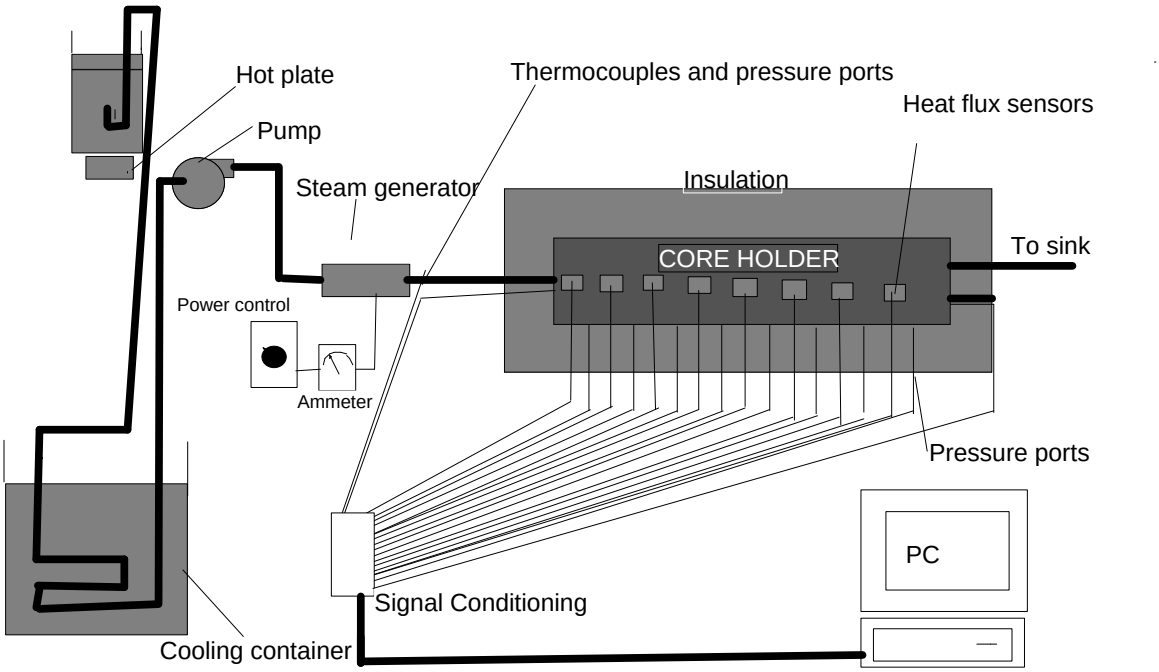

Figure 2.17: Modified experimental apparatus for single water injection line.

and thermocouples

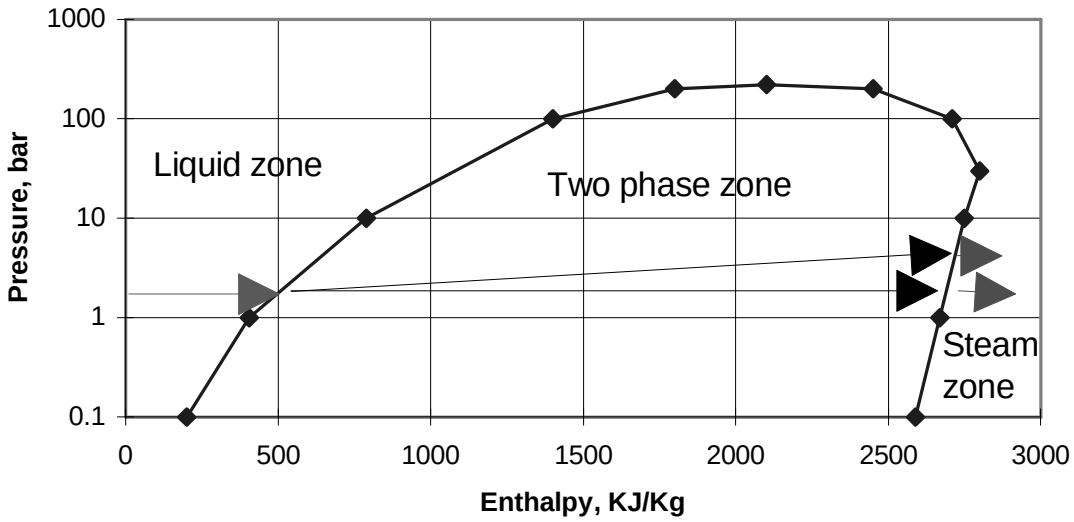

Figure 2.18: Saturation dome from Cengel and Boles (1989).

Water temperature increased linearly as heat was supplied until the two-phase zone was reached. Once in the two-phase zone the water temperature no longer changed.

However the steam quality increased from zero to one as the heat supplied was increased as shown in Figure 2.19. At the steam saturation line the steam quality reached its maximum of one and, once again, the fluid temperature should increase linearly with respect to the supplied heat. This method allows us to divide the saturation dome into steps correlated with the heat supplied by the steam generator to obtain the steam mass flowing fractions *x* as follows:

$$power = c + mx \tag{2.16}$$

where *c* and *m* are constants. Or:

$$amps = c + mx \tag{2.17}$$

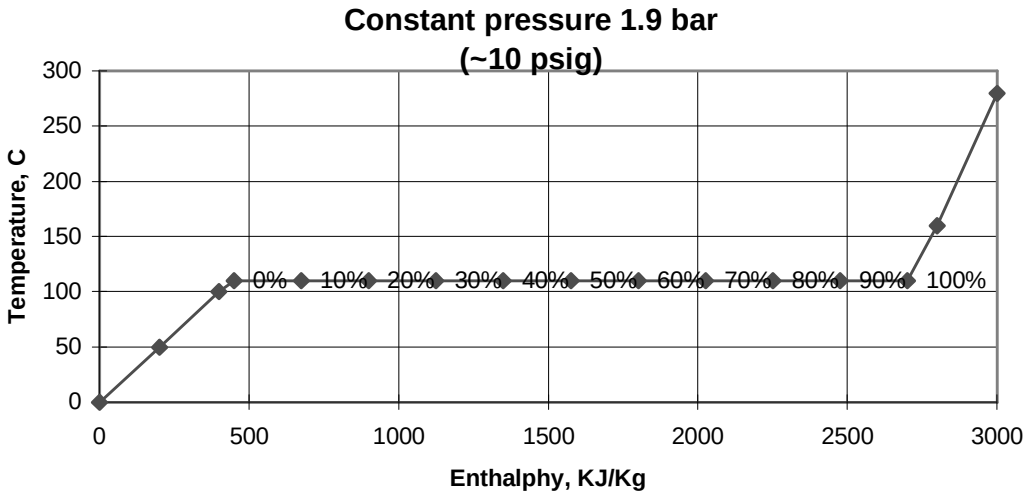

Figure 2.19: Steam quality increases from zero to one as the heat supplied is increased.

Solving for *x* we obtain:

$$x = \frac{amps - c}{m} \tag{2.18}$$

The constants were evaluated at the saturated liquid line where x=0 and at the saturated vapor line where x=1.

As in Method I, the relative permeabilities to steam and water can be calculated with Equations (2.14) and (2.15) respectively. This method assumes constant heat transfer rate from the steam generator to the fluid and constant heat losses in the lines throughout the two-phase zone. The advantage of this method with respect to Method I is that it simplifies the experimental apparatus, as well as the procedure and calculations. It is no surprise that two of the most recent experiments to measure steam-water relative permeabilities, Piquemal (1994) and Sanchez and Schechter (1987), used a variation of this single injection technique. Piquemal (1994) calibrated heat losses in the steam generator under conditions of one-phase (liquid) flow while Sanchez and Schechter (1987) used an adiabatic steam generator.

Figure 2.20 shows data collected in a period of 4630 minutes from experiment "Exp. 4-4-97", illustrating the temperature variation at the core inlet as a function of the heat supplied to the steam generator. The plot eventually flattens at about 300 watts meaning the onset of two-phase flow (saturated liquid, x=0). The peak at about 430 watts could be wrongfully interpreted as the onset of saturated vapor. However, Figure 2.21 shows a peak in the core inlet pressure at the same power setting implying that the fluid was still in the two-phase zone (Figure 2.18, inclined arrow line). After the peak the water temperature remains fairly constant up to the end of the experimental data.

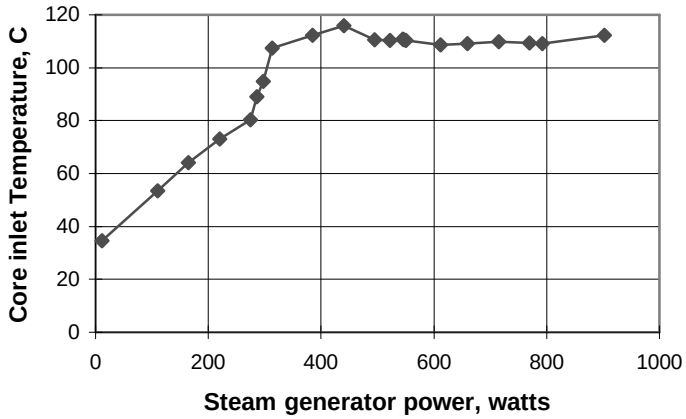

Figure 2.20: Water temperature versus heat supplied from experiment "Exp. 4-4-97".

Figure 2.20 and Figure 2.21 show partial results as the core failed before superheated conditions were reached. In view of this partial agreement between theory and experimental data, Equation (2.18) is believed to be an adequate estimate of the steam flowing fraction.

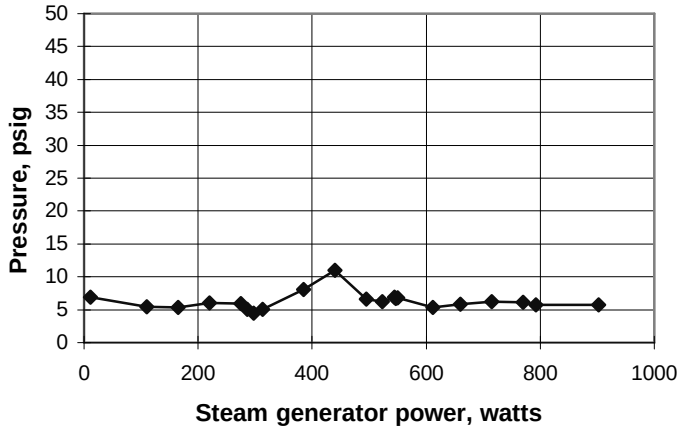

Figure 2.21: Water pressure versus heat supplied from experiment "Exp. 4-4-97".

It is important to note that with this method as well as with Method I the average steam flowing fraction must be calculated downstream to a point along where the saturation profile is flat. Thus in both cases, Method I and II, this average flowing fraction can be calculated from an energy balance of the downstream radial heat losses.

2.5 CONCLUSION

Analysis of the X-ray CT images showed that on the average the core samples were homogenous in porosity.

Considerable care must be exercised to obtain accurate saturation measurements with the X-ray CT scanner. Because of its high resolution, liquid density variation with temperature can be detected, which may give erroneous results in the evaluation of the saturation. Hence for two-phase flow experiments, the scans to compare the liquid phase must be at elevated temperatures as close as possible to saturated conditions. However caution should be taken to avoid reaching the two-phase zone, as this would give even more unreliable saturation measurements.

The variation of absolute permeability as a function of temperature was found to be small. Similarly, absolute permeability measurements remained fairly constant while the water

injection flow rate was varied. Small variations can be attributed to the precision of the pressure transducers. From these results, and for the purpose of this experiment, we concluded that absolute permeability does not vary with temperature or flow rate.

Two methods were investigated to obtain steam fractional flows in order to measure relative permeability for steam-water flow in a homogeneous porous medium. The first method was the simultaneous injection of steam and hot liquid water to the core. At steady state, it was difficult to differentiate the conditions between the two injection fluids. It was also difficult to differentiate the condition of a point downstream of the core injection lines.

The second method, called for the injection of water to while it underwent a phase change. In both methods the heat added or lost could only be approximated, which created uncertainty in the results. The single injection line method is preferred as it simplifies the experimental set up, as well as the procedure and calculations.

3 ESTIMATION OF RELATIVE PERMEABILITY FUNCTIONS FROM BOILING EXPERIMENTS

This research project is being conducted by Research Assistant, Marilou Guerrero, Dr. Cengiz Satik, and Prof. Roland Horne. The objective of this study is to estimate the relative permeability functions for steam-water systems by inverse modeling, using data from the boiling experiments (Section 1).

3.1 SUMMARY

This report discusses the procedure of parameter estimation by inverse modeling. The parameter estimation simulator, ITOUGH2, was used to estimate linear relative permeability and capillary pressure function parameters. These parameters are the immobile water saturation, RP(1), maximum water saturation RP(3), and maximum capillary pressure CP(1). Preliminary results showed that the best estimates are: RP(1)=0.202, RP(3)=0.900, and CP(1)=9700 Pa.

3.2 NUMERICAL MODEL FORWARD CALCULATION USING TOUGH2

In the previous quarter, an actual boiling experiment was modeled using TOUGH2 (details of the experiment are described in Section 1). Simulation results were obtained from combinations of different relative permeability and capillary pressure functions.

In this quarter, the model was modified to better represent the actual experiment. The core was divided into ten layers whose nodes coincided with the locations of the measuring ports along the Berea core in the experiment. In the experiment, a 0.5 cm thick layer of epoxy covered the core, outside of which was a 0.16 cm thick layer of insulation. An ambient gridblock was added to the whole system to model heat losses around the core. The external conditions were modeled by giving the ambient gridblock an infinitesimal porosity (0.0001) and a relatively small permeability of 1×10^{-20} m^2. The ambient block was made to have the same properties as the insulation in terms of specific heat and thermal conductivity, and was given a huge volume. To maintain a constant pressure boundary on the top layer of the core, the topmost gridblock layer was given a very large volume and porosity, and a permeability ten times greater than the permeabilities of the epoxy and insulation blocks.

3.3 FORWARD CALCULATION USING TOUGH2

To better mimic the observed values, the parameters in the linear relative permeability and capillary pressure functions were manipulated. These were the same parameters used later in the inverse modeling. In addition, the material properties were given more

appropriate values and the power input was increased from 6.2 J/s to 10.2 J/s. Figures 3.1 - 3.6 show comparisons of the observed and simulated data with respect to distance from the heater and time elapsed.

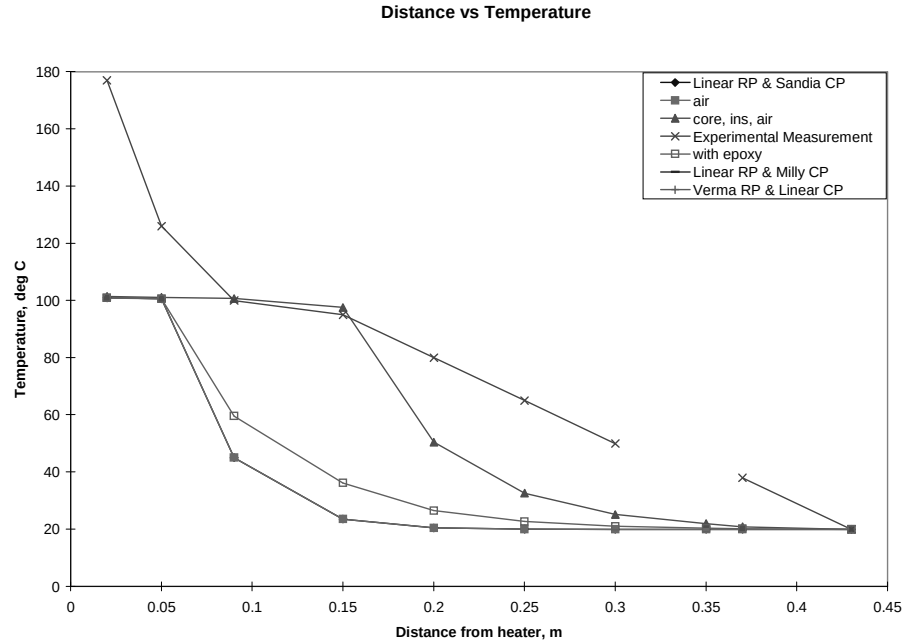

Figure 3.1: Temperature vs. Distance from Heater

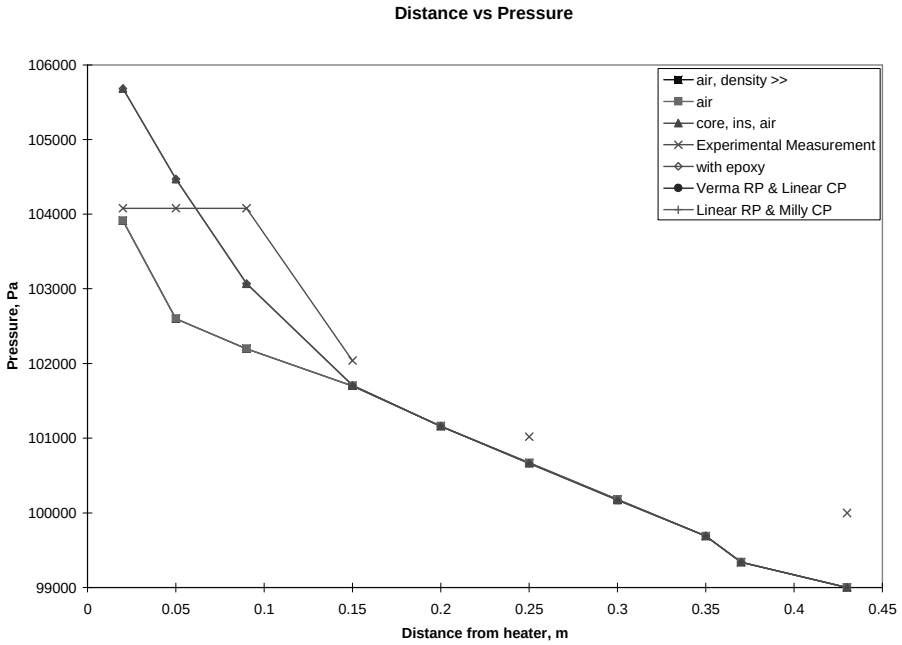

Figure 3.2: Water Pressure vs. Distance from Heater

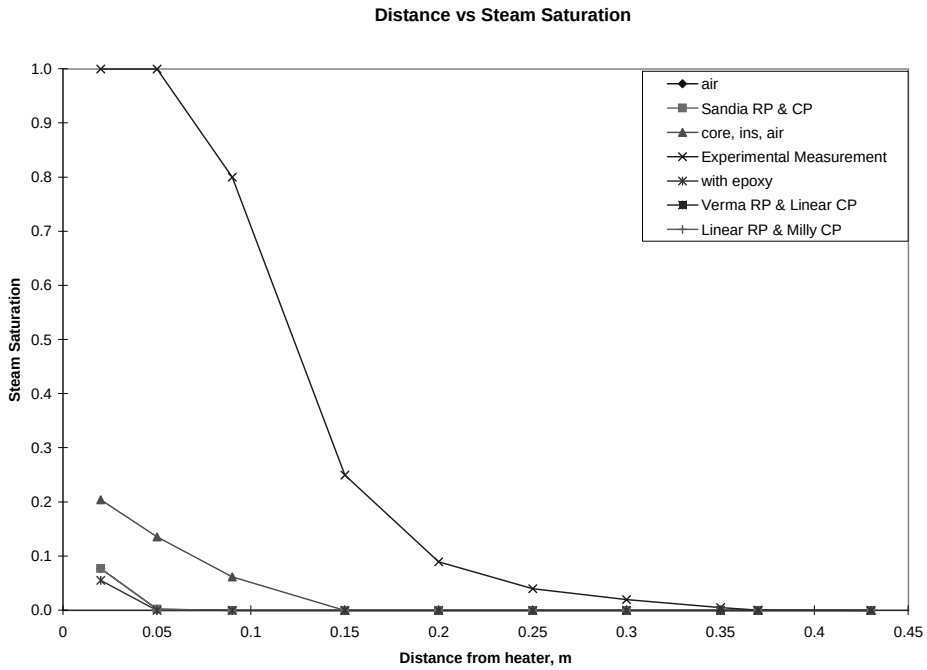

Figure 3.3: Steam Saturation vs. Distance from Heater

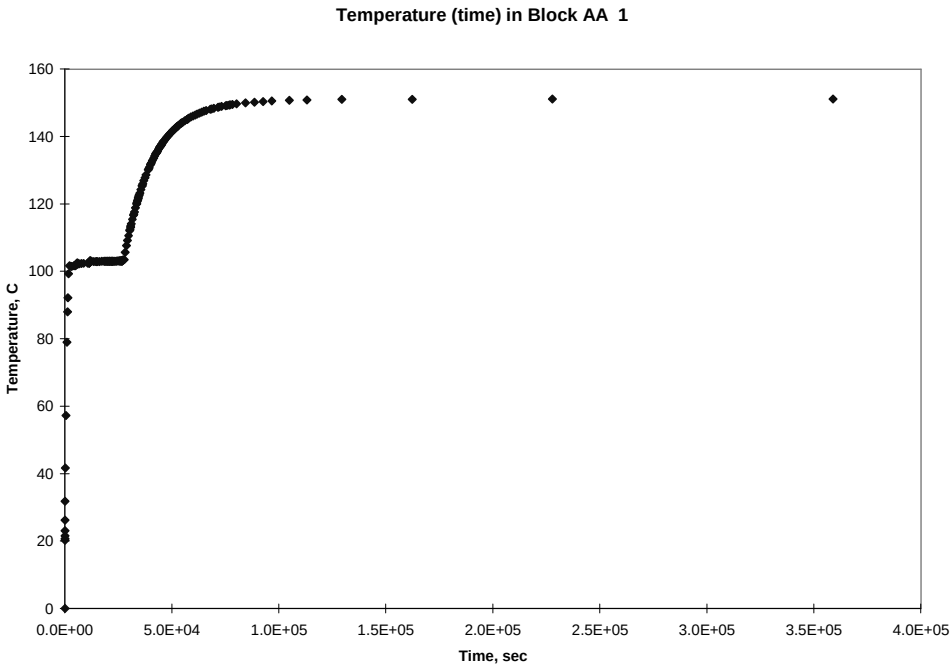

Figure 3.4: Temperature vs. Time

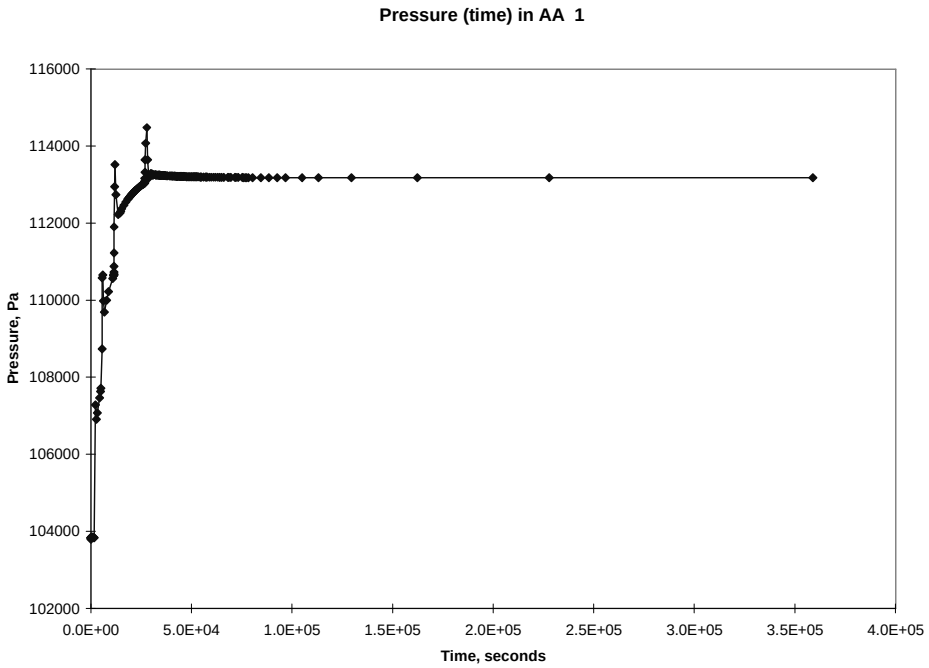

Figure 3.5: Water Pressure vs. Time

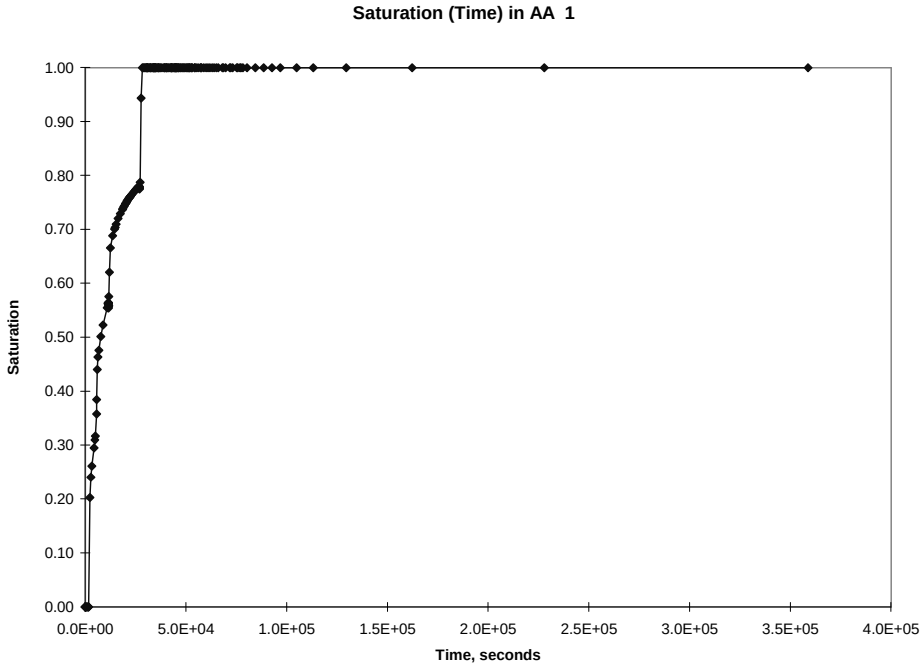

Figure 3.6: Steam Saturation vs. Time

3.4 PARAMETER ESTIMATION BY INVERSE MODELING

The inverse problem, or the estimation of parameters from measured data in this case, was solved by minimizing the differences between the observed and simulated system responses. Simulated results were obtained from TOUGH2, and were compared with observed data (ITOUGH2 input file) for model calibration. Results of initial ITOUGH2 runs showed that the best estimates for the linear relative permeability and capillary pressure model are: RP(1)=0.202, RP(3)=0.900, and CP(1)=9700 Pa.

3.5 FUTURE WORK

Further inverse modeling will be carried out for other combination of relative permeability and capillary pressure functions. Also, another experiment will be conducted to measure the pressures, temperatures and saturations more precisely.

4 APPLICATION OF X-RAY CT SCANNING IN SATURATION AND POROSITY MEASUREMENT

This project is being conducted by Research Assistant Meiqing He, Dr. Cengiz Satik and Professor Roland Horne. The aim of this project is to identify and characterize fractures in geothermal rocks by using X-ray computer tomography (CT) equipment. Previously, we studied the fundamental physics of the CT technique and proposed two ways of porosity calculation, in the current quarter a comparison of two methods was undertaken.

4.1 REVIEW OF TWO METHODS FOR POROSITY AND SATURATION CALCULATION

Conventionally, porosity and saturation are obtained from CT measurement after saturating the porous medium with contrast agents, e.g. water and air are most commonly used. There are two sets of CT scans needed to calculate porosity. One is the dry scan (CT_{dry}), which is conducted when the porous medium is fully saturated with air; the other is the wet scan (CT_{wet}), which is conducted after the porous medium has been saturated with water. Then the porosity is obtained by

$$\phi = \frac{CT_{wet} - CT_{dry}}{CT_{water} - CT_{air}} \tag{4.1}$$

To calculate saturation another set of CT scans ($CT_{p_1p_2}$) is required when the two phases, p_1 and p_2 are coexisting in the porous medium. The saturation is given by

$$S_{p_1} = \frac{CT_{p_1p_2} - CT_{p_2r}}{CT_{p_1r} - CT_{p_2r}} \tag{4.2}$$

$$S_{p_2} = 1 - S_{p_1} \tag{4.3}$$

where the subscript r refers to rock.

Another approach is to use the dual energy scan technique. In this technique, two sets of scans at different energy levels are made to same slices of the object (Akin, *et al*. 1996). The two sets of linearly independent data measured at two energy levels E_1 and E_2, CT^1 and CT^2, are represented in the following equations:

$$CT^1 = (1-\phi)CT^1_{Matrix} + S_{p_1}\phi CT^1_{p_1} + (1-S_{p_1})\phi CT^1_{p_2} \tag{4.4}$$

$$CT^2 = (1-\phi)CT^2_{Matrix} + S_{p_1}\phi CT^2_{p_1} + (1-S_{p_1})\phi CT^2_{p_2} \tag{4.5}$$

The CT numbers of phase 1 and phase 2 at two energy levels can be calibrated beforehand and the matrix CT number can also be determined when preliminary knowledge of the porosity is supplied. For example, if we assume a core is fully saturated with air, the matrix CT number can be calculated by using approximate porosity and saturation.

Hence, we can solve for the porosity and saturation by using following equations:

$$\varphi = \frac{\left(CT^2 - CT^2_{matrix}\right)\left(CT^1_{ph1} - CT^1_{ph2}\right) + \left(CT^2_{ph2} - CT^2_{ph1}\right)\left(CT^1 - CT^1_{matrix}\right)}{\left(CT^1_{ph1} - CT^1_{ph2}\right)\left(CT^2_{ph2} - CT^2_{matrix}\right) + \left(CT^2_{ph1} - CT^2_{ph2}\right)\left(CT^1_{matrix} - CT^1_{ph2}\right)} \tag{4.6}$$

$$S_{ph1} = \frac{\left(CT^1 - CT^1_{matrix}\right)\left(CT^2_{ph2} - CT^2_{matrix}\right) - \left(CT^2 - CT^2_{matrix}\right)\left(CT^1_{ph2} - CT^1_{matrix}\right)}{\left(CT^2 - CT^2_{matrix}\right)\left(CT^1_{ph1} - CT^1_{ph2}\right) - \left(CT^1 - CT^1_{matrix}\right)\left(CT^2_{ph1} - CT^2_{ph2}\right)} \tag{4.7}$$

4.2 EXPERIMENTS

4.2.1 Calibration of single phase CT number

We scanned a 4.5 inch glass container when it was filled with air and water at different energy levels, as shown in Table 4.1. These numbers will be substituted as reference numbers in the calculation.

Table 4.1 CT Number measured at different energy levels (kev)

	140 kev	120 kev	110 kev	100 kev
air	-995	-993	-992	-991
water	-40	-19	-44	-19

4.2.2 Core scanning

A Berea sandstone sample was used to investigate the two methods. We scanned the Berea sandstone when the core was dry, then did another scan after the core had been fully saturated. The CT numbers measured during the different situations are CT_{dry} and CT_{wet} respectively. The porosity can thus be calculated by the conventional way described in Section 4.1.

The dual energy scans were done at 140 kev and 110 kev when the core was fully saturated with water. One hundred percent water saturation was assumed in determining CT_{matrix} and porosity by the dual energy method presented in Section 4.1.

4.3 RESULTS AND DISCUSSION

4.3.1 Results

In this section we will present in detail how we obtained the approximate matrix CT number and how the subsequent porosity results varied. The numbers presented in the charts were all averaged within a circle of 40 pixels in radius.

In Fig. 4.1, we used the first slice porosity profile obtained by the conventional way as the porosity approximation to determine the matrix CT number. That matrix CT number value was used in the next 41 slices to recalculate the porosity. In Fig. 4.2, we used the porosity values from the 33rd slice instead to determine the matrix CT number.

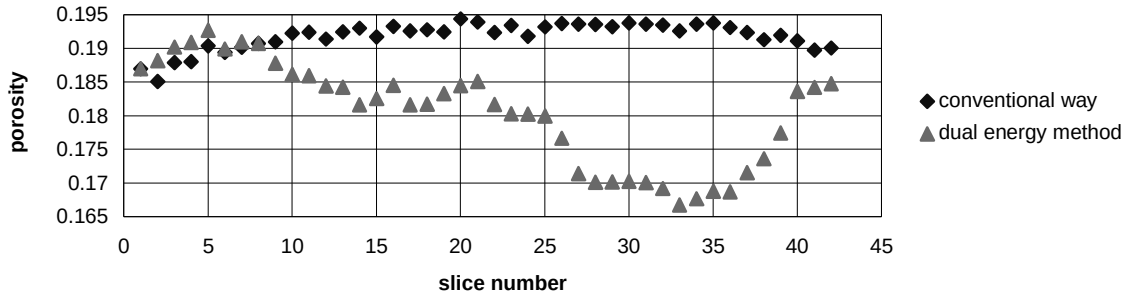

Figure 4.1 Porosity profile (using porosity profile from 1st slice)

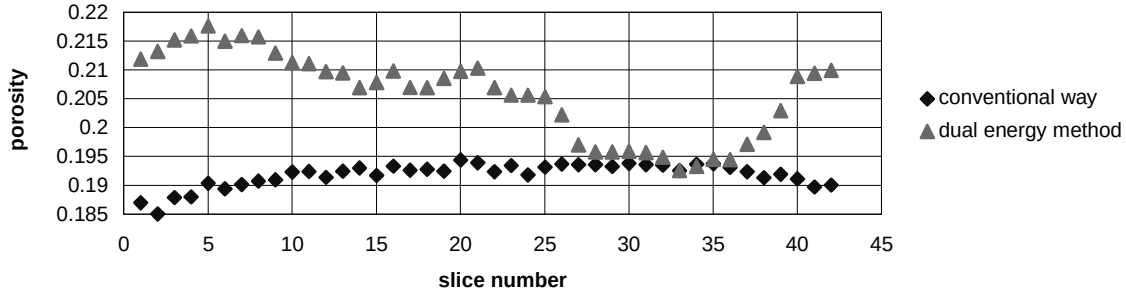

Figure 4.2 Porosity profile (using porosity profile from 33rd slice)

We then averaged the local porosity within a slice over 42 slices, denoting it as $\bar{\varphi}$. For the standard method $\bar{\varphi} = 0.191858$. We substituted this value into the first and the 33rd

slice respectively to calculate the matrix CT number, and hence recalculated the porosity. Results are shown in Fig. 4.3 and Fig. 4.4.

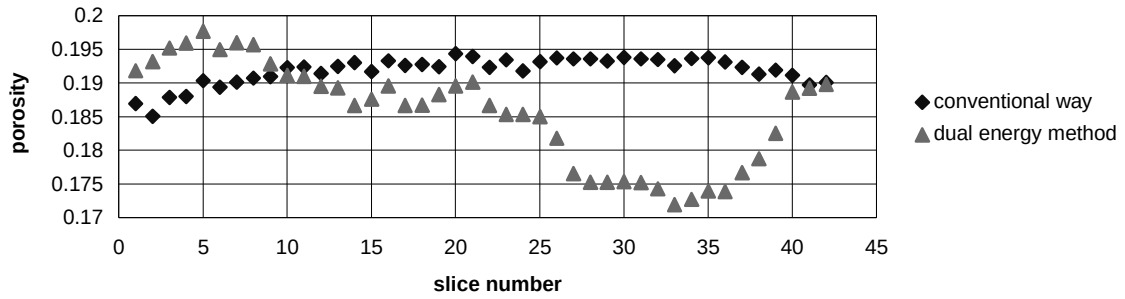

Figure 4.3 Porosity profile (substituting $\overline{\varphi}$ into the first slice)

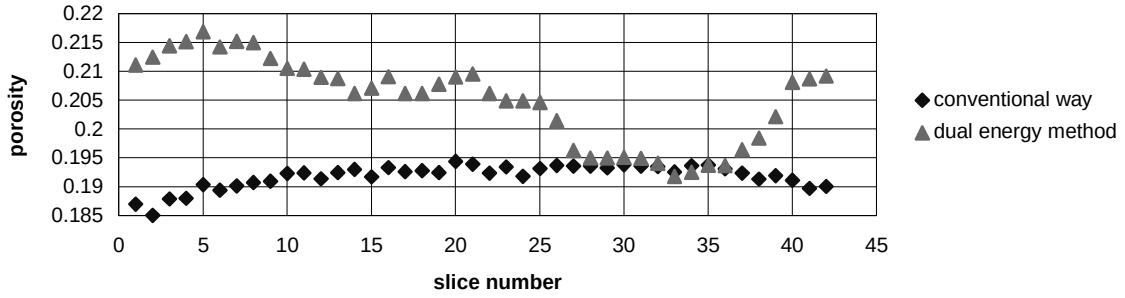

Figure 4.4 Porosity profile (substituting $\overline{\varphi}$ in the 33rd slice)

We also tried determining $\overline{\varphi}$ from the standard method using the first slice scan, and calculated the matrix CT number as a result . From this we obtained an averaged matrix CT number $\overline{CT}_{matrix} = 1484.6$. The result is shown in Fig. 4.5.

The values of $\overline{\varphi}$ that resulted from the five different ways of determining matrix CT number area summarized in Table 4.2.

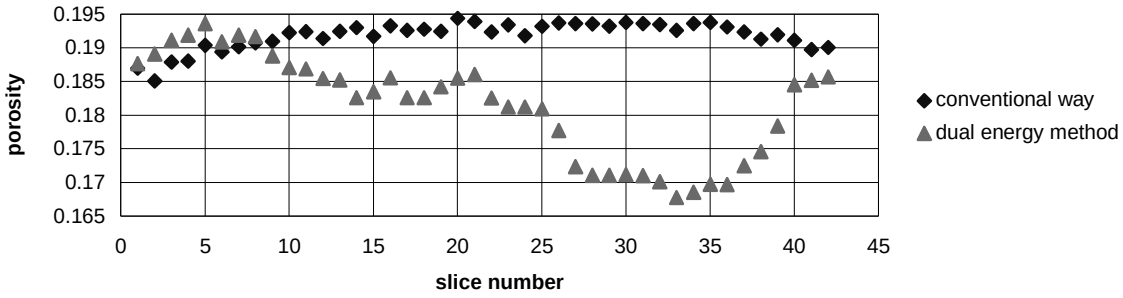

Figure 4.5 Porosity profile (substitute $\bar{\varphi}$ in the first slice, apply $\overline{CT}_{matrix} = 1484.6$ to the rest of the slices)

Table 4.2 Table of $\bar{\varphi}$

	Standard method	dual energy in Fig. 4.1	dual energy in Fig. 4.2	dual energy in Fig. 4.3	dual energy in Fig. 4.4	dual energy in Fig. 4.5
$\bar{\varphi}$	0.191858	0.180509	0.205852	0.205097	0.185572	0.181462

4.3.2 Discussion

Compared with results from the standard approach, the porosity profiles obtained from the dual energy method show larger deviations. There are dips located between the 27th slice and 37th slice, which are a strong indication of beam hardening effect along the longitudinal direction of the core. In the standard method, the beam hardening effect is canceled by the subtraction of CT_{wet} and CT_{dry}, whereas in the dual energy method the CT numbers measured at different energy levels suffer independent beam hardening effects which can not be canceled.

Note in Fig. 4.5 that the result from applying a constant matrix CT number does not affect the profile very much. This can also be seen by comparing the $\bar{\varphi}$ values, 0.180509 and 0.181462. Thus we could simplify our calculation by applying constant porosity and matrix CT number. This is a benefit of the relative homogeneity of Berea sandstone. In addition, we need to note that although the porosity profile from the standard method is flatter, the $\bar{\varphi}$ values from the dual energy method are within an acceptable fluctuation range, 5% maximum deviation compared to the standard method values. Therefore the dual energy method does provide another way of determining porosity.

4.4 FUTURE WORK

We will apply the dual energy method to Geysers core. One aspect of such an investigation is the need to deal with the heterogeneity typical of Geysers cores. Also we would like to address the way of calibrating the CT number of the saturating agents we plan to use.

5 BOILING IN A VERTICAL FRACTURE; THERMAL FRONT PROPAGATION

This project is being conducted by Research Assistant Robert DuTeaux, Dr. Cengiz Satik and Prof. Roland Horne. The goal of this project is to optimize strategies for injection into fractured geothermal reservoirs.

5.1 INTRODUCTION

The near-term goal of this research has been to develop an experiment to investigate the heat transfer associated with water boiling in a fracture. The experimental apparatus described in the previous report was developed further this past quarter and some preliminary experiments have been conducted. Plans to address the longer-term goal of numerical simulation have also been outlined.

5.1.1 Progress

Two single-phase experiments were conducted and one boiling experiment was attempted. The apparatus worked well in the two single-phase liquid experiments, and the assembly was tested for leaks and integrated with a data acquisition system. However, the initial boiling experiment was unsuccessful, primarily due to high heat losses from the assembly that allowed it to cool too quickly to initiate boiling in the fracture, and also because a leak in the outer vacuum insulation region pulled water out of the fracture (the annulus between two concentric glass tubes). These results suggested that some modifications in the sealing of the assembly and some changes in the experimental procedure would improve the experimental design.

5.1.2 Single-phase liquid experiment

The propagation of a thermal front was recorded in two preliminary single-phase experiments. The experimental apparatus illustrated in Figure 5.1 was employed with thermocouples at two vertical levels in the fluid filled annulus, and at corresponding locations inside the core of the apparatus. The core was initially at room temperature, with thermocouples placed at the inner surface of the tube, and at one and two centimeters radially inward within the sand-filled center. Cold water was pumped through the assembly at 50 ml/min while thermocouples measured the fluid temperatures between the glass tubes and at locations within the core. The thermocouples were placed at vertical locations of 21.5 and 26.5 centimeters above the insulation in the bottom of the core, and temperatures were recorded as the cooling water flowed up through the annulus of the concentric glass tubes. Figure 5.2 plots some of the data recorded from the second experiment conducted in this manner.

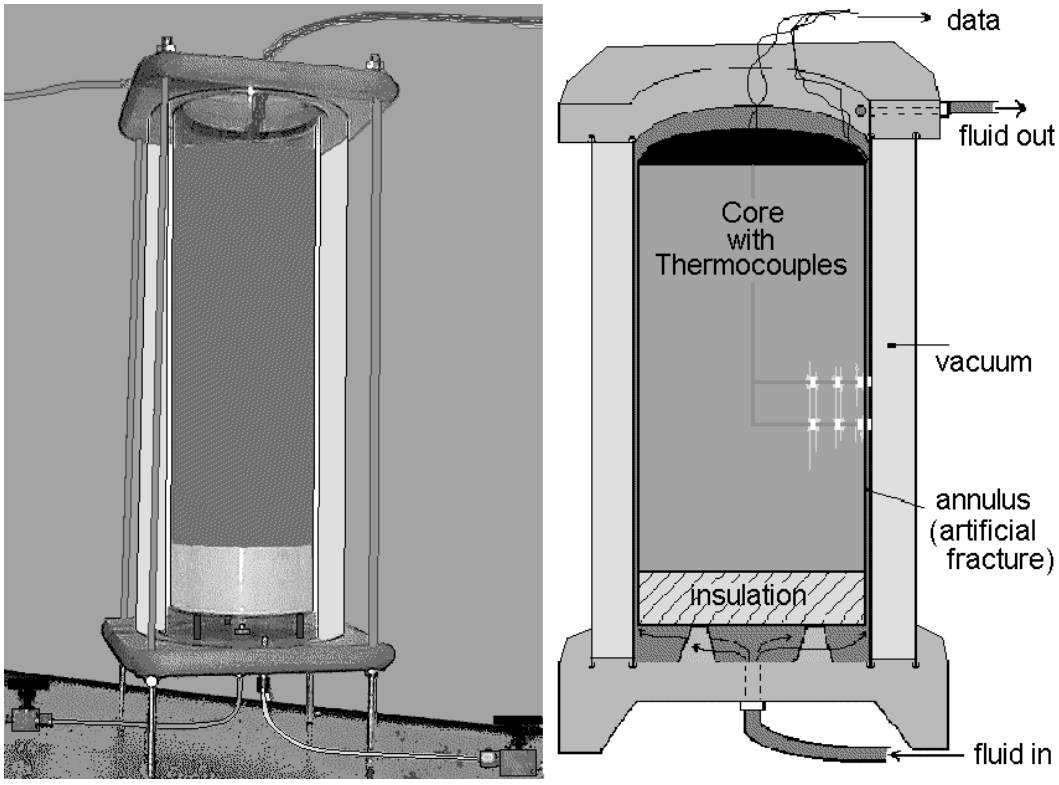

Figure 5.1 Experimental apparatus.

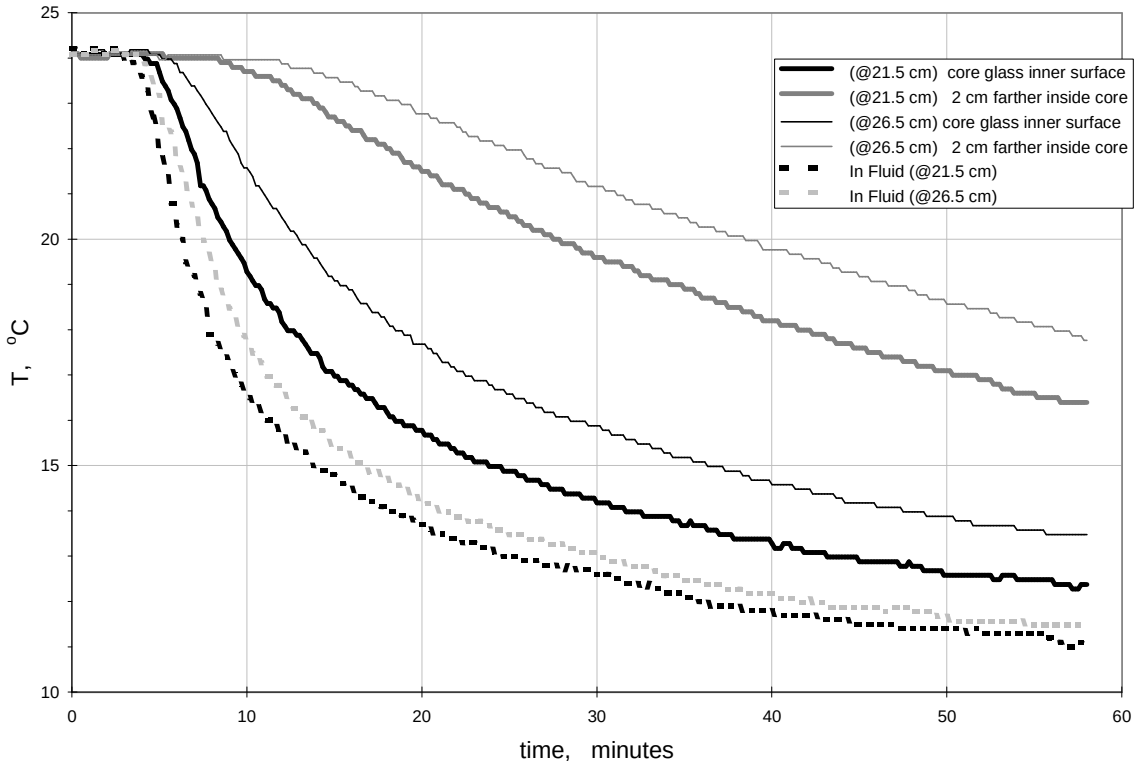

Figure 5.2 Temperature measurements in the fluid and radially inside the core.

Figure 5.2 illustrates the propagation of the cooling front in the direction of flow and also plots the temperature decline radially inward away from the fracture with time. The dashed traces are the fluid temperatures at two vertical locations and the other traces are temperatures inside the core at the same corresponding vertical locations. In this experiment the cold fluid flowed upward from the base of the apparatus and progressively cooled the core from the bottom to the top. Therefore, the locations of the thermocouples are specified by distance from the insulation in the bottom of the core assembly.

5.1.3 Boiling experiment

In the first attempt to conduct a boiling experiment sand was heated to 150 ^{o}C in an oven and poured into the core of the assembly around the previously placed thermocouples, rather than placing the entire core of the assembly in the oven as had been originally intended. This was done because of the difficulty of handling a heated core. Since the glass tube was initially at room temperature, the outer diameter of the core conducted heat from the sand, and the glass cooled within a few minutes to just less than 100 ^{o}C. This occurred as water at 90+ ^{o}C was being pumped into the apparatus, so the water in the fracture did not flash to steam. From these results changes in procedure were suggested and a number of potential improvements are planned. Also, as mentioned previously, a leak in the insulating vacuum developed and modifications for sealing the assembly are planned.

5.2 THE NEXT STEPS

5.2.1 Experimental plan

The fundamental plan has been to heat the core in an oven, place it in the assembly, and then inject water at just below a saturated temperature. As the heat provided by a higher temperature core conducts to the fracture, water boils in the annulus, and thermocouples measure the temperatures and monitor the upward propagation of the interface between the liquid and vapor. In a manner similar to the data collected from the single-phase experiment, the thermocouples were designed to record the thermal signature of a propagating thermal front in the direction of fluid flow. A series of this type of experiments at different flow rates has been planned for the next quarter of study.

5.2.2 Numerical modeling

Plans have also been developed to employ the code TOUGH2 to compare with empirical observations of two phase experiments as data is obtained.

6 THE ROLE OF CAPILLARY FORCES IN THE NATURAL STATE OF FRACTURED GEOTHERMAL RESERVOIRS

This study is currently being undertaken by Prof. Roland Horne and Research Assistant Nemesto Noel A. Urmeneta. The objective of the work is to determine the influence of capillary forces in the creation of a fractured vapor-dominated geothermal reservoir.

6.1 INTRODUCTION

Much of the experimental work which pertains to geothermal systems has involved studies on porous media, even though most geothermal reservoirs are observed to be fracture dominated. It is unclear whether a porous medium model is adequate in describing a geothermal reservoir since there are some situations where the fractured nature of the reservoir cannot be ignored. One case involves the injection of cold brine (normally around 160°C) as a means of pressure support or for environmental reasons. If the geothermal system were to behave like a homogeneous porous medium, the thermal front would advance uniformly with the cooler fluid sweeping away the heat from the rock. In reality, this will not be the case. There will be a preferential flow through the fractures and even though there is transfer of heat by conduction from the rock to the cold water passing through the fractures, the injected water will arrive much sooner than in the case of a porous medium. Because of this problem, a dual porosity model is often invoked. Instead of treating the reservoir as homogeneous, fractures are introduced by dividing the system into two types of interacting porous media as in Fig. 6.1. The matrix is assigned a permeability, k_m, and a porosity, ϕ_m, while the fracture is assigned a higher permeability, k_f, and a higher porosity, ϕ_f.

In a dual porosity model, the question of how heat is being transferred from the rock matrix to the fluid flowing in the fractures has been investigated. Previous works include those by Bodvarsson (1969, 1972), Drummond and McNabb (1972) and Nathenson (1975). The objective of this work was to further our understanding by investigating how heat and mass transfer is affected by capillary forces. To address this issue, it is worthwhile to investigate the heat pipe effect. The heat pipe mechanism (Eastman, 1968) allows the upward movement of heat in a system that exhibits a very small temperature gradient. Since this problem is reasonably understood from earlier work, studying the heat pipe mechanism enabled us to understand the effect of capillary pressure on the behavior of fractured reservoirs.

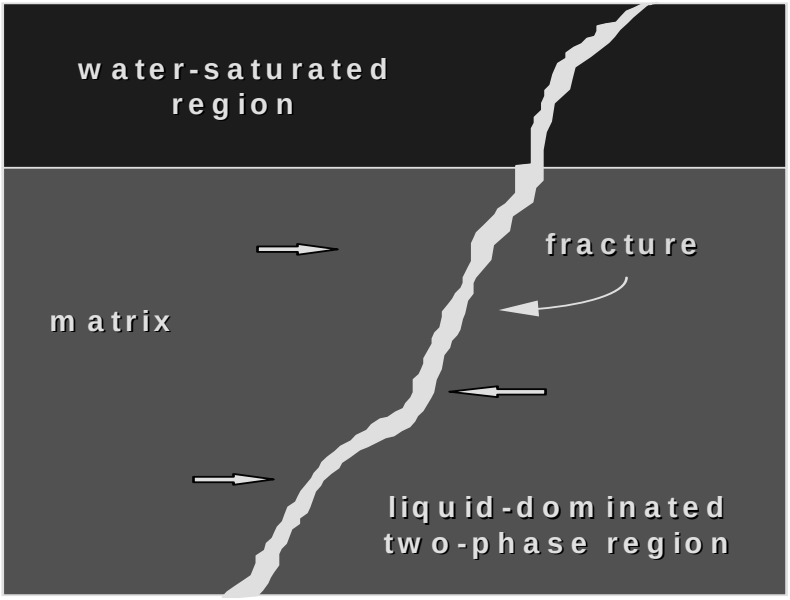

Figure 6.1: A dual porosity model.

White et al. (1971) proposed a conceptual model of a vapor-dominated geothermal reservoir. The model has a deep-seated convecting brine which is heated by a magmatic heat source. On top of this convecting brine is a two-phase region whose vapor and liquid phases undergo counterflow convection. This two-phase region is separated from the overlying zone of meteoric water and steam condensate by a caprock. For liquid-dominated systems, most of the conceptual models likewise invoke the presence of a caprock. Such is the case for the Tongonan geothermal reservoir in the Philippines (Grant and Studt, 1981) and the Wairakei geothermal field in New Zealand (Grindley, 1965).

Sondergeld and Turcotte (1977) did experimental studies on two-phase thermal convection in a porous medium. They were able to observe that a counterflowing two-phase zone can be stable beneath a water-saturated zone (Fig. 6.1). This experimental result suggests that geothermal reservoirs need not have to have a caprock. How is this possible? Will the presence of fractures destabilize the arrangements of fluids? What will be the influence of capillarity in permitting this configuration? One of the objectives of this study was to explore the stability of a water-saturated zone overlying a two-phase zone. The investigation on the stability of such systems was limited, however, to the case of a liquid-dominated two-phase reservoir.

To answer these questions, a numerical investigation was conducted utilizing the commercial program TETRAD (version 12). The approach utilized in this study involved the concept of building complexity. To start with, a one-dimensional numerical model was built in order to examine the heat pipe effect. This model was then extended to two

dimensions. With this model the effect of capillary forces on heat and mass transfer as well as on stability was investigated by varying the capillary pressure curves.

6. 2 PRELIMINARY WORK

Prior to the development of the two-dimensional numerical model used in this study, a one-dimensional numerical model was constructed in order to duplicate some of the results obtained by previous investigators who worked on heat pipes. Having a one-dimensional numerical model that conforms with experimental and theoretical results reinforces the validity of the model. Being confident with the one-dimensional model, the two-dimensional model was constructed in a similar fashion to the one-dimensional case. Since the numerical model now had two dimensions, the question of which differencing scheme, whether a five-point differencing scheme or a nine-point differencing scheme, is appropriate for the numerical model was raised. Likewise, the type of capillary pressure functions to be used in the study had to be determined.

One-Dimensional Model

The one-dimensional model consisted of a 7 m × 50 m × 1 m block and ten 7 m × 50 m × 50 m blocks stacked on top of each other as shown in Fig. 6.2. The model represents a homogeneous system and the properties assigned to each block are summarized in Table 6.1. The topmost block was given a very large volume in order to impose a constant pressure and saturation condition at the top. The blocks were initially saturated with water. With a 1 W/m^2 heat flux imposed at the bottom block, numerical simulation was carried out until steady state conditions were attained.

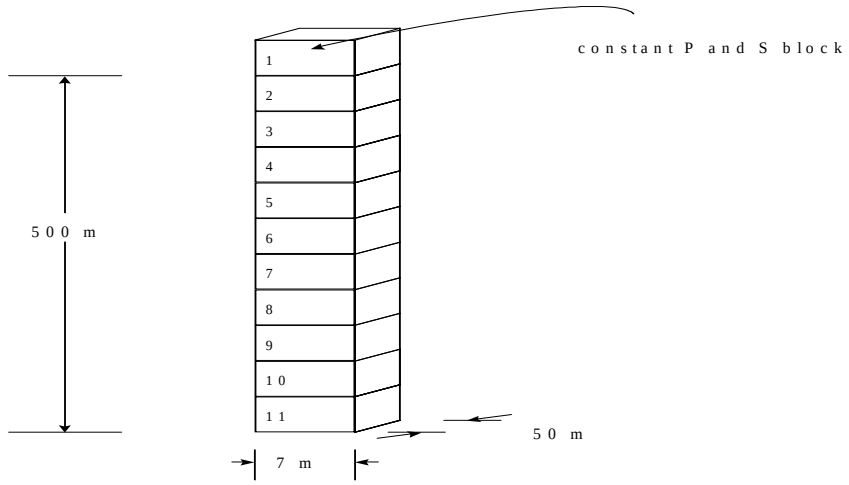

Figure 6.2: One-dimensional model of a heat pipe.

Table 6.1: Parameters of the one-dimensional model.

Property	Block 1 (Large volume element)	Blocks 2 - 11 (Matrix blocks)
Porosity	0.8	0.1
Permeability (mD)	2000	0.5
Rock density (kg/m^3)	2643	2643
Rock conductivity (W/m-°C)	2.88	2.88
Rock specific heat (kJ/kg-°C)	1.0718	1.0718
Heat flux (W/m^2) - block 11		1.0
Relative permeability	$k_{rl} = (S)^3$ $k_{rv} = (1\text{-}S)^3$	$k_{rl} = (S)^3$ $k_{rv} = (1\text{-}S)^3$

The saturation profile indicated that we had two-phase conditions at a depth of 175 m (block no. 5) down to the bottom. Results indicated that in this two-phase region vapor rises up to block no. 5 while liquid trickles from block no. 5 down to the bottom. There was a counterflow of the liquid and the vapor phases within the two-phase zone. A plot of the dimensionless heat flux versus saturation is shown in Fig. 6.3. The analytical solution was derived for the cubic relative permeability curves (Table 6.1) using the same procedure as Bau and Torrance (1982). The dimensionless heat fluxes for each block were calculated. The points do not plot exactly on the line representing the analytical solution but instead lie just to the right of it. One possible explanation for this is that the heat transfer mechanism in this one-dimensional system involves both convection and conduction, whereas the analytical solution does not take conduction into account. The graph however shows that we were able to produce a liquid-dominated heat pipe since the water saturations were above the saturation corresponding to the maximum heat flux, in this case, 0.26.

Two-Dimensional Model

With the existing one-dimensional model, a two-dimensional grid was produced by having 20 grid blocks in the x direction instead of just having one and maintaining the number of layers in the z direction. The grid system is shown in Fig. 6.4.

The model had dimensions of 7 m × 501 m × 50 m and consisted of 220 blocks. The first two columns had a length of 0.01 m, the third column had a length that is twice that of the previous one and this progression continued until the seventh column had a length of 0.32

m. The eighth column had a length of 0.36 and the remaining 12 columns had a length of 0.5 m. The depth and width of each grid block was 50 m. The blocks in the first layer were assigned very large volumes and were fully saturated with water hence these large volume blocks were termed the aquifer blocks. The rest of the blocks were labeled as matrix blocks. The same properties outlined in Table 6.1 were assigned to this two-dimensional numerical model. The same heat flux of 1 W/m^2 was delivered to the blocks at the bottom layer.

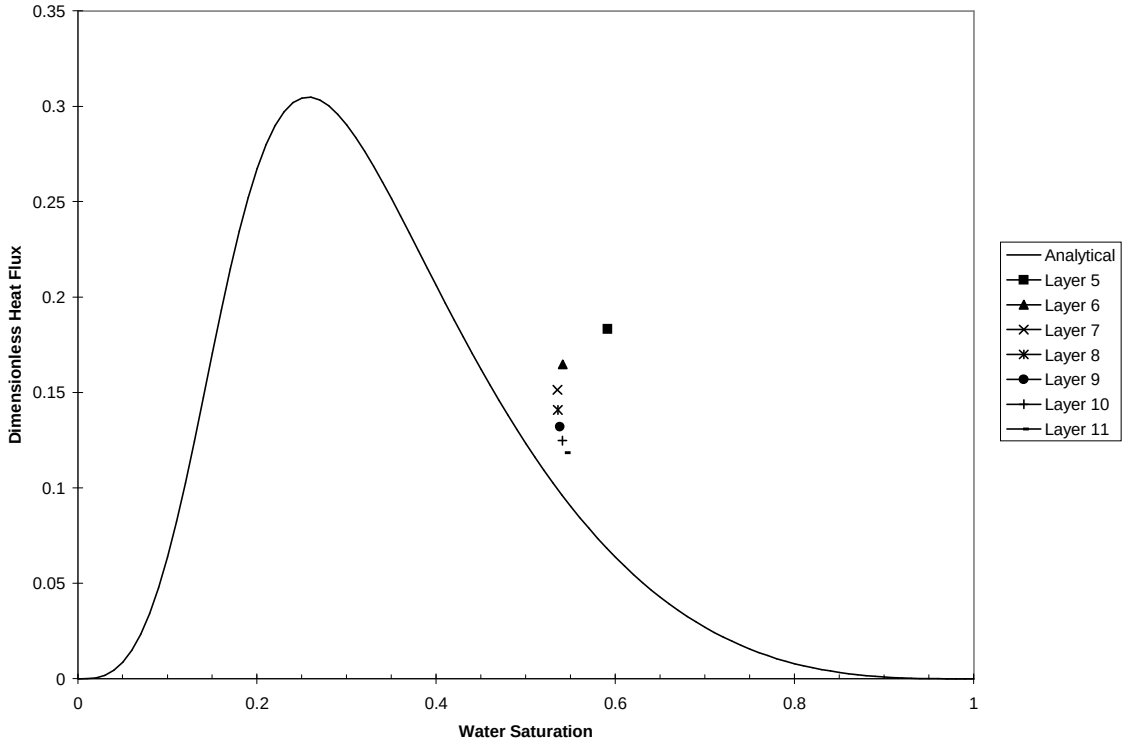

Figure 6.3: Plot of the dimensionless heat flux versus saturation for a cubic relative permeability curve.

To achieve steady state, the model was ran up to a time of 4×10^6 days. The results showed no variation in the temperature, pressure and saturation values along the *x* direction in all the layers. Even though a two-dimensional grid was used, the system behaved like the one-dimensional case due to the fact that the system was homogeneous. As such, the temperature, pressure and saturation profiles for the two-dimensional case are exactly the same as those in the one-dimensional case. Likewise, the graph of the non-dimensional heat flux as a function of water saturation looks exactly like Fig. 6.3. With this two-dimensional model, the stability of a water-dominated region over a liquid-dominated two-phase system was demonstrated.

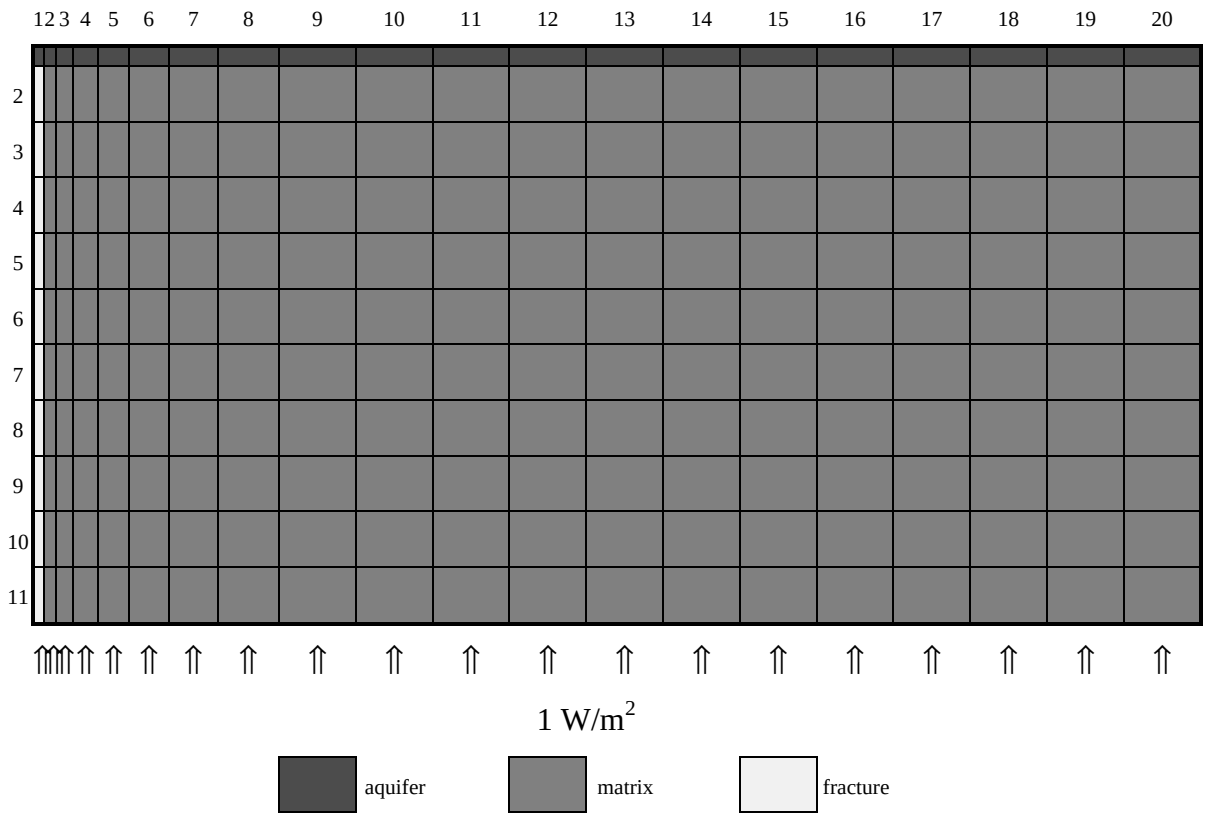

Figure 6.4: The 20 × 11 × 1 block model.

The fact that the two-dimensional model with uniform matrix properties was able to duplicate the behavior of the one-dimensional model reinforces the validity of both models as well as that of the simulator itself. After having shown that a water-dominated region can be stable over a liquid-dominated two phase region, the next question was, how would this stability be affected by the presence of fractures.

The reason why the grid was designed as in Fig. 6.4 was in order to model a fracture on the left-hand side. Hornbrook and Faulder (1993) modeled a fracture by having large blocks (10 m wide) which were assigned a porosity of 0.0001 in order to simulate a 1 mm fracture. The fracture in this case was modeled by having blocks which were thin (0.01 m wide) and which were given a porosity of 0.5 in order to simulate a 0.005 m fracture. By specifying a larger permeability and porosity to the blocks in column 1 as compared to the matrix blocks (Fig. 6.4), a fracture at the left-hand side of the model was created. This two-dimensional model with both fracture and matrix blocks was the one used in the investigation.

Five-point versus nine-point differencing schemes

The standard approach in numerical simulation work is to make use of the five-point differencing scheme in the discretization of the differential equations describing reservoir flow. In a two-dimensional grid, the flow in and out of a computational grid point is influenced by the points directly to the sides, above and below it. With a higher order differencing scheme, such as a nine-point, the four computational grid points along the diagonals are also taken into account. Pruess (1991) indicated that although there are cases where the five-point differencing scheme is appropriate, there are certain situations where the nine-point differencing scheme is better. Pruess showed that a higher-order differencing scheme substantially diminishes the grid orientation effects. The study done by Hornbrook and Faulder (1993) asserted that the nine-point differencing scheme was more appropriate. The question then was, which differencing scheme is appropriate for the two-dimensional system in this study?

To address this issue, we made use of a 5 × 1 × 11 block numerical model whose properties were similar to the model described earlier. The dimensions, however, were 25 m × 50 m × 501 m. Using the five-point differencing scheme, the steady state solution was simulated. Three other simulation runs utilizing the five-point differencing scheme were performed using different models. The second model had 10 blocks in the *x* direction while the third and fourth ones had 14 and 18 blocks, respectively. The numerical runs indicated that with the five-point differencing scheme, the results obtained were consistent. The steady state solution was independent of the grid system used.

A second set of simulation runs was conducted using the same set of models. However, this time the nine-point differencing scheme was utilized. Results indicated that the steady state solution for each run was dependent on the grid system used.

A comparison between experimental and numerical results was done in order to further examine the applicability of the five-point differencing scheme. The experimental results obtained by Bau and Torrance (1982) for a porous bed with permeability of 8.5 d were simulated using a radial grid model. The centerline temperatures obtained from experiments were compared to those obtained from the numerical model where a five-point differencing scheme was used. Fig. 6.5 shows that the numerical results replicate the experimental results especially in the two-phase regions.

From these observations, we determined that the five-point differencing scheme was more appropriate than the nine-point differencing scheme for this type of problem. Hence, all the subsequent numerical runs used the five-point differencing scheme.

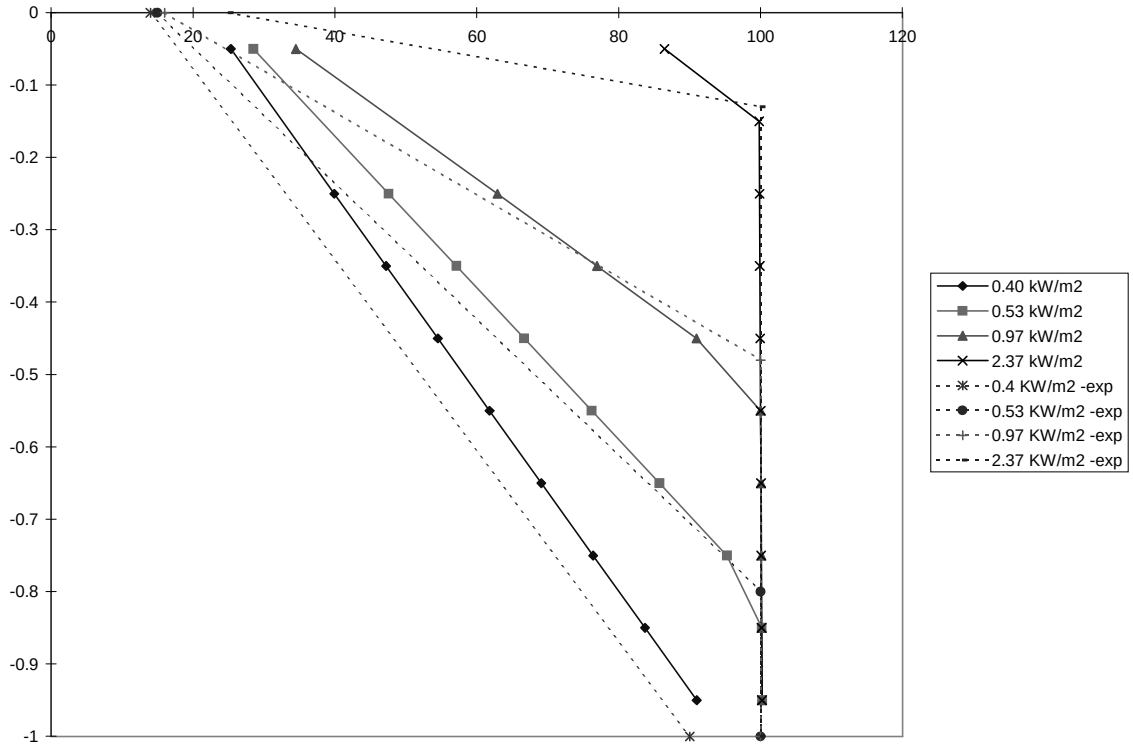

Figure 6.5: A comparison between the centerline temperatures obtained from Bau and Torrance's (1982) experiment and the radial grid numerical model.

Capillary pressures

The two-dimensional model described earlier has three different domains - the aquifer, the matrix and the fracture blocks. A primary issue in the study was to determine the appropriate capillary pressure functions for the different domains.

For the aquifer blocks, since we wanted all of the liquid to be mobile we imposed zero capillary pressure. For the matrix blocks, the capillary pressure curves were similar to those derived from a typical Geysers isotherm. For the fracture blocks, we first thought that since the fracture has a large equivalent pore size, the capillary pressure would approach zero and hence would be independent of the saturation. Simulation runs were carried out using constant capillary pressures that ranged from 0 to 200 kPa for the fracture blocks. The simulation runs did not converge to a steady state solution. Hence, a linear capillary pressure function was used instead. A linear capillary pressure function was also utilized by Pruess (1985) and Hornbrook and Faulder (1993) for the fracture blocks in their studies.

6.4 RESULTS

We have established that a water-saturated zone can remain stable over a liquid-dominated two-phase region. The question is, what would happen to this stability when a fracture is added to the system. Will the system become unstable and flip over? What role do capillary forces have on the observed stability? If the system is in fact stable even with the presence of the fracture, how do capillary forces affect the heat and mass transfer between the fracture and the matrix? These issues will be discussed in this section.

The two-dimensional model was used. The matrix and fracture properties are summarized in Table 6.2. There were five models used in this study, each differing in the type of capillary pressure function imposed on the fracture blocks.

Table 6.2: Parameters of the two-dimensional model used in the simulation.

Property	Aquifer	Matrix	Fracture
Porosity	0.8	0.1	0.5
Permeability (md)	2000.0	0.5	50.0
Rock density (kg/m^3)	2643	same	same
Rock conductivity (W/m-°C)	2.88	same	same
Rock specific heat (kJ/kg-°C)	1.0718	same	same
Heat flux (W/m^2) - blocks 201-220		1.0	1.0
Relative permeability	$k_{rl} = (S)^3$	same	same
	$k_{rv} = (1\text{-}S)^3$	same	same

The matrix capillary pressure is described by the equation

$$p_c = 100\left(S^{-1/0.6} - 1\right)^{0.4} \qquad (6.1)$$

while the fracture capillary pressure is described by the equation

$$p_{cf} = -A(S) + A \qquad (6.2)$$

where S is the water saturation and A is the maximum fracture capillary pressure in kPa. There was no capillary pressure function assigned to the aquifer blocks. The capillary pressure functions used in the different models are shown in Table 6.3.

Table6.3: The capillary pressures used for the different models.

Model	Aquifer	Matrix	Fracture
I	0	$p_{cm} = 0$	$p_{cf} = 0$
II	0	$p_{cm} = 100\left(S^{-1/0.6} - 1\right)^{0.4}$	$p_{cf} = -200S + 200$
III	0	$p_{cm} = 100\left(S^{-1/0.6} - 1\right)^{0.4}$	$p_{cf} = -100S + 100$
IV	0	$p_{cm} = 100\left(S^{-1/0.6} - 1\right)^{0.4}$	$p_{cf} = -50S + 50$
V	0	$p_{cm} = 100\left(S^{-1/0.6} - 1\right)^{0.4}$	$p_{cf} = 0$

Using TETRAD version 12, simulations were carried out for up to 4×10^6 days in order to reach steady state.

For Model I where no capillary pressures were prescribed, the two-phase region underneath the water-saturated zone collapsed. The temperature, pressure and saturation profiles indicate that we have a water-saturated region occupying the entire system.

For Model II where a van Genuchten type of capillary pressure curve was prescribed for the matrix blocks and a linear capillary pressure curve with a maximum value of 200 kPa was prescribed for the fracture blocks, an oscillatory behavior was observed for the temperature, pressure and saturation profiles with time. The period of oscillation was 3.5 cycles per 1×10^5 days.

For Model III where the maximum capillary pressure in the fracture blocks is 100 kPa, a water-saturated region remains stable on top of the two-phase zone. The saturation distribution is shown in Fig. 6.6. It was not unlikely that the fracture blocks, being highly permeable, would easily become saturated with water from the overlying four layers of fully water-saturated rock matrix. The numerical results obtained, however, indicate otherwise. In fact, the fracture has an average steam saturation of 80% while the adjacent matrix blocks are on the average 75% saturated with water.

The dimensionless heat flux for the fracture blocks in the two-phase region were calculated. These points when plotted versus saturation would lie towards the vapor-dominated heat pipe solution (Fig. 6.7). It can be noted that the point from Layer 5 is far from the analytical curve. This point actually belongs to the block that serves as an interface between the water-saturated and the vapor-dominated regions. Figure 6.7 indicates that the fracture blocks in Layers 6 to 11 form a vapor-dominated heat pipe.

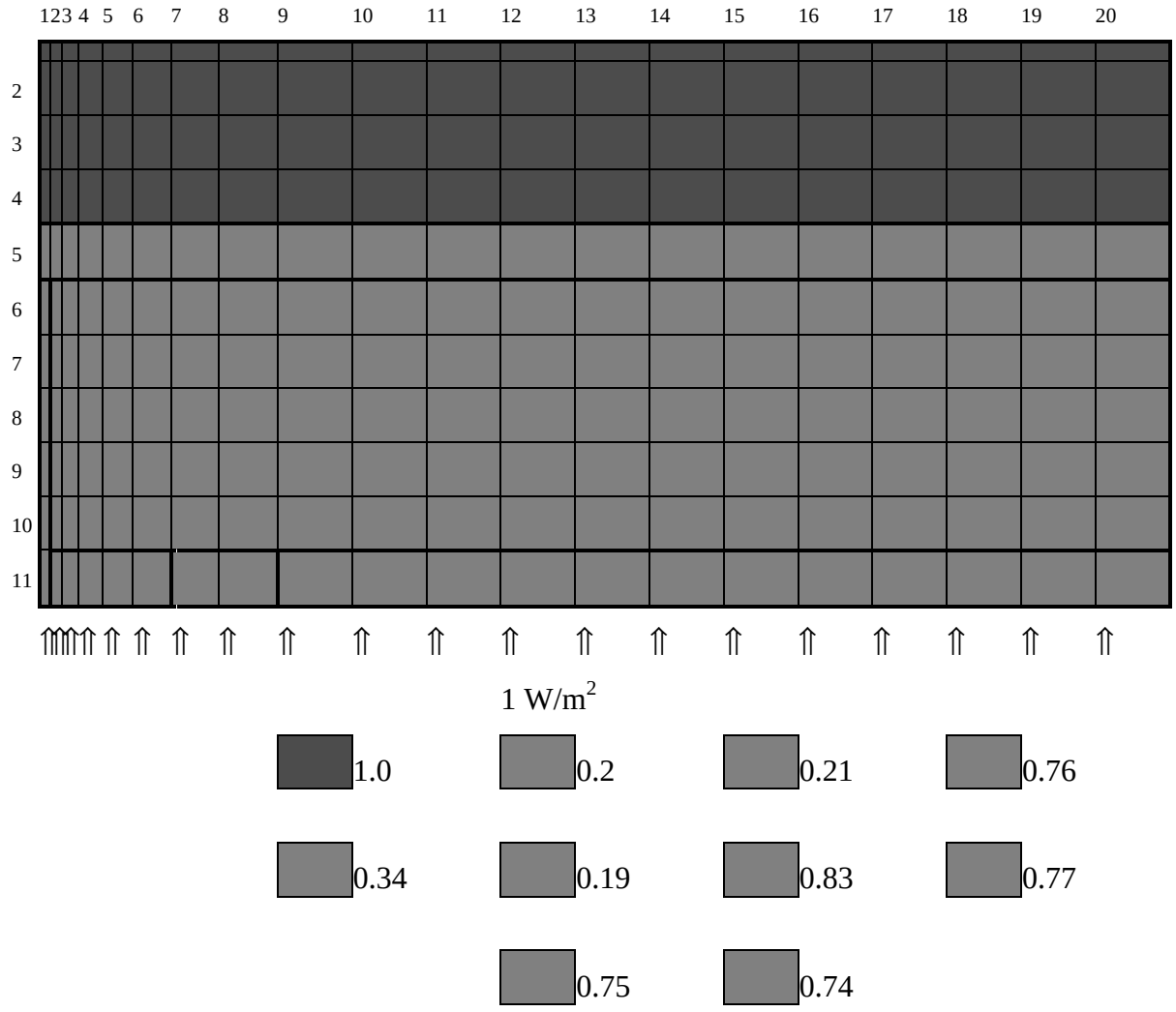

Figure 6.6: Liquid saturation distribution for Model III.

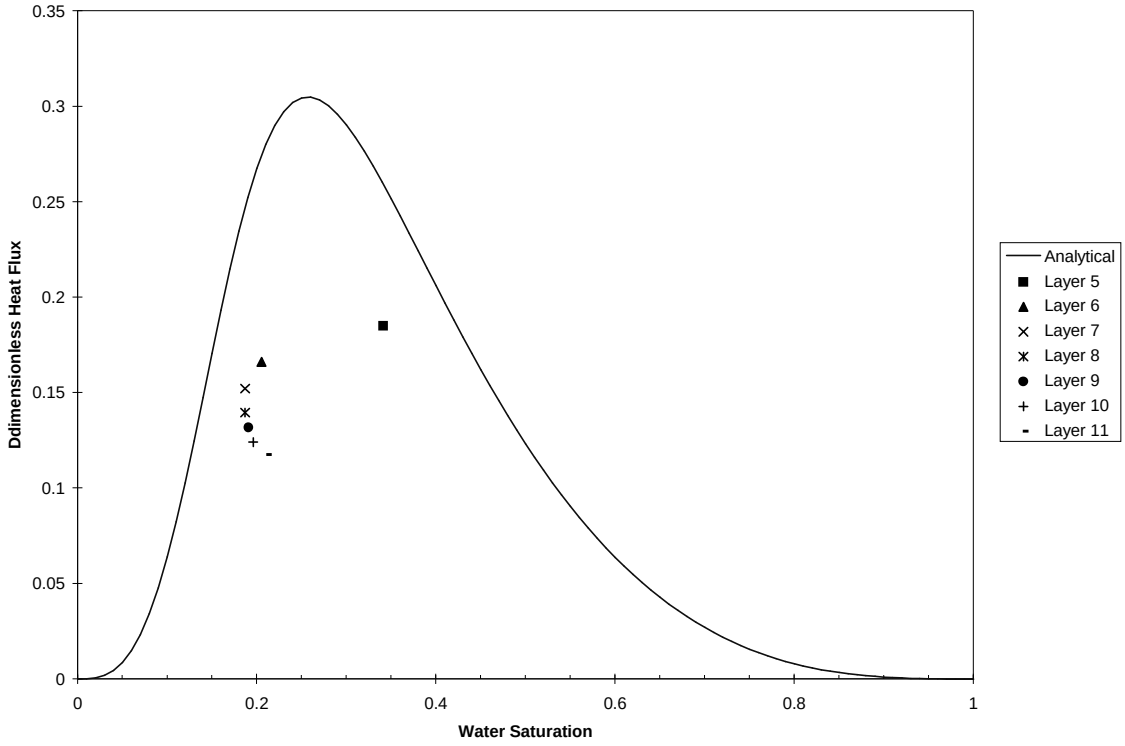

Figure 6.7: Plot of the dimensionless heat flux versus saturation for the fracture blocks of Model III.

For Model IV, the maximum capillary pressure in the fracture blocks was decreased by 50 kPa. The saturation field is shown in Fig. 6.8. When the maximum capillary pressure in the fracture blocks was decreased to 50 kPa, the amount of water retained in the fracture blocks decreased. The average steam saturation in the fracture blocks within the two-phase zone is 85%. Correspondingly, the amount of fluid in the matrix blocks increased. The average water saturation in the matrix blocks became 93%. Calculations for the heat flux within the fracture blocks would indicate that we do have a vapor-dominated heat pipe (Fig. 6.9). The points are much nearer to the line representing the analytical solution.

The results from Model V show that the matrix blocks are almost entirely water-saturated (Fig. 6.10). Examination of the pressure, temperature and saturation distribution within the fracture blocks and the plot of the dimensionless flux versus saturation (Fig. 6.11) indicates that the fracture is actually a vapor-dominated heat pipe. When compared to Model IV, the saturations are not significantly different.

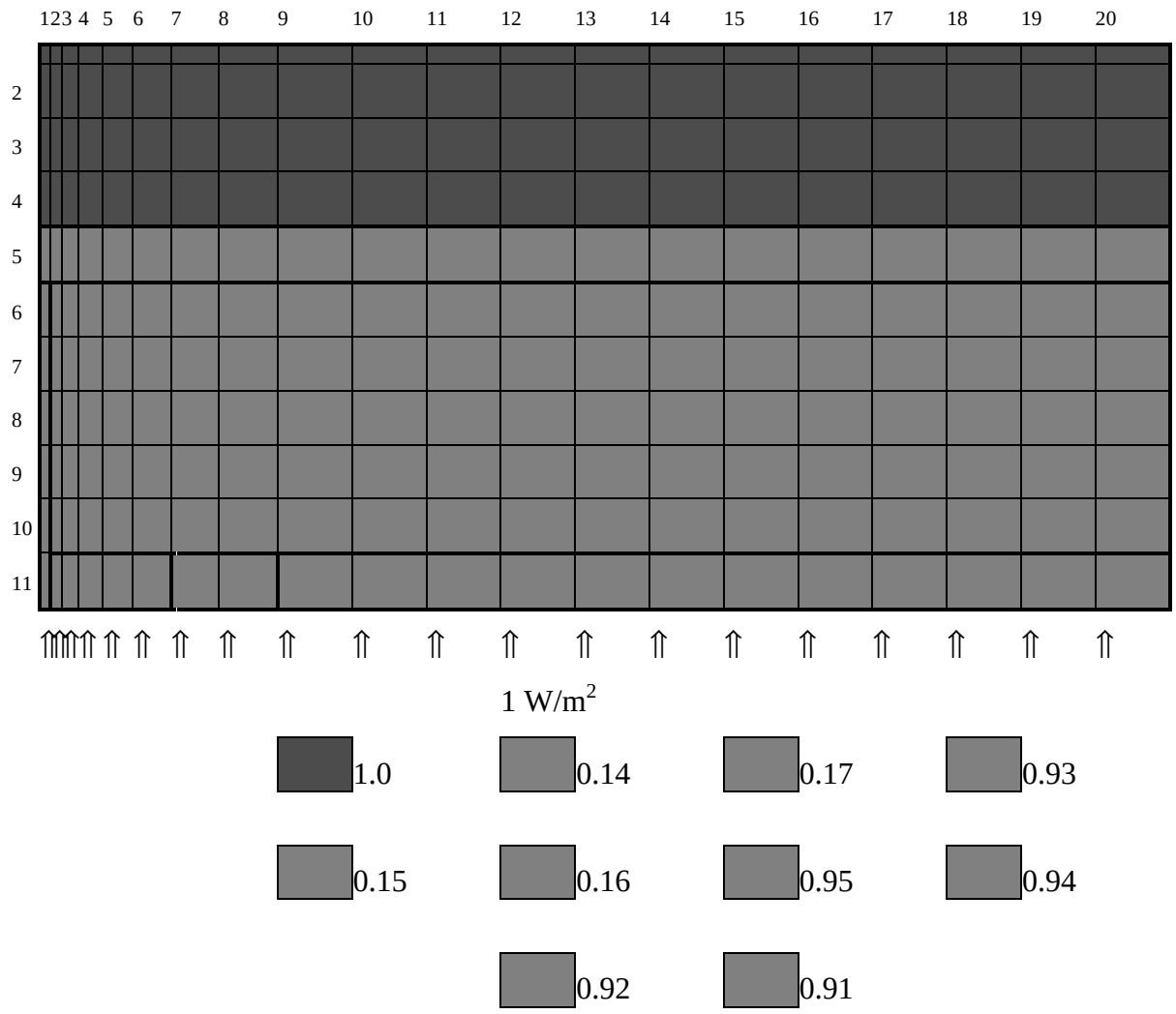

Figure 6.8: Liquid saturation distribution for Model IV.

On the issue of stability, Model I indicates that numerically it is not possible to maintain a water-saturated region on top of a liquid-dominated two-phase fractured reservoir if no capillary pressure functions are specified for both the matrix and the fracture blocks. However, Model V gave the result that even if no capillary pressures were specified for the fracture blocks, a small two-phase zone could still exist below a water-saturated zone. Combining these observations, we can say that having zero capillary pressures in the matrix blocks would destroy the stability of water over a liquid-dominated two-phase region.

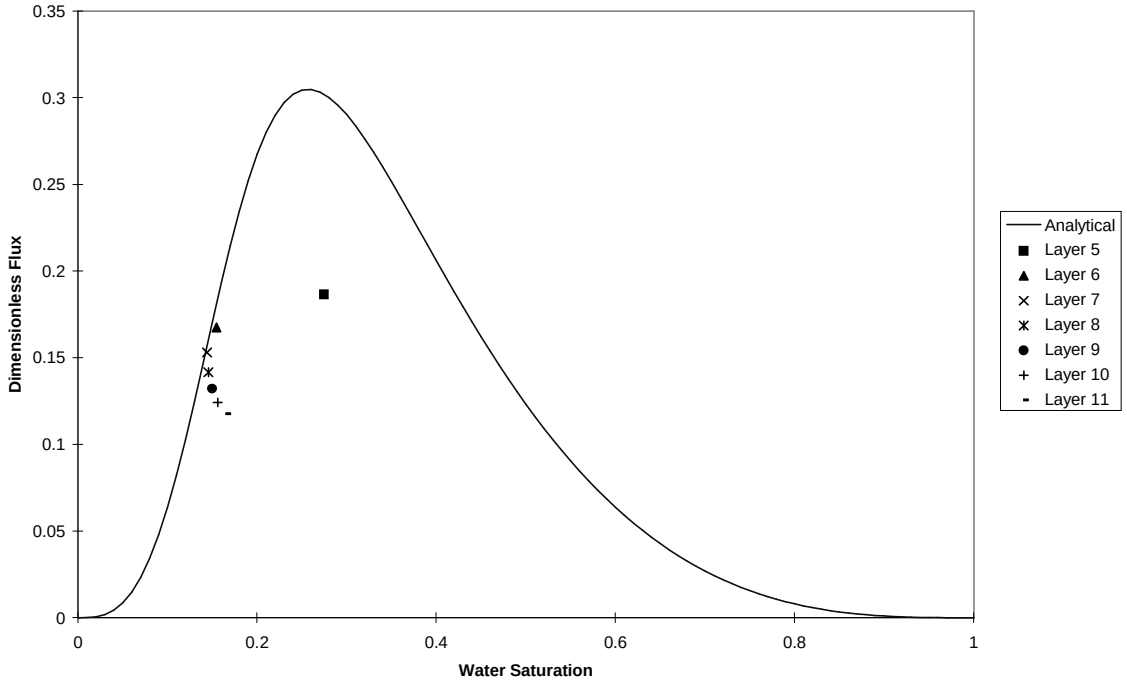

Figure 6.9: Plot of the dimensionless heat flux versus saturation for the fracture blocks of Model IV.

From Models III to V, it can be observed that the fracture acted like a heat pipe and as the maximum capillary pressure specified on the fracture blocks is diminished, the average steam saturation increases. This is due to the fact that capillary forces tend to suck the liquid phase into the pores of the porous medium. In the presence of vapor, the capillary forces through adsorption would induce capillary condensation and the net effect is to have a higher liquid saturation. Having zero capillary pressures in the fracture increases the heat pipe effect. This is good if we want to look at it in terms of heat transfer. Heat is transmitted more effectively since the mode of heat transfer is through convection. Steam rises through the fractures and on reaching the water-saturated region, loses energy, condenses and trickles down. Liquid is also transferred from the matrix blocks into the fracture where it boils off and rises as steam. Numerical results indicate that as the capillary pressure in the fracture is diminished, the rate at which liquid is transferred from the matrix into the fracture is increased. Likewise, the steam flux going through the fracture is increased. In other words, convection is enhanced and so is heat transfer.

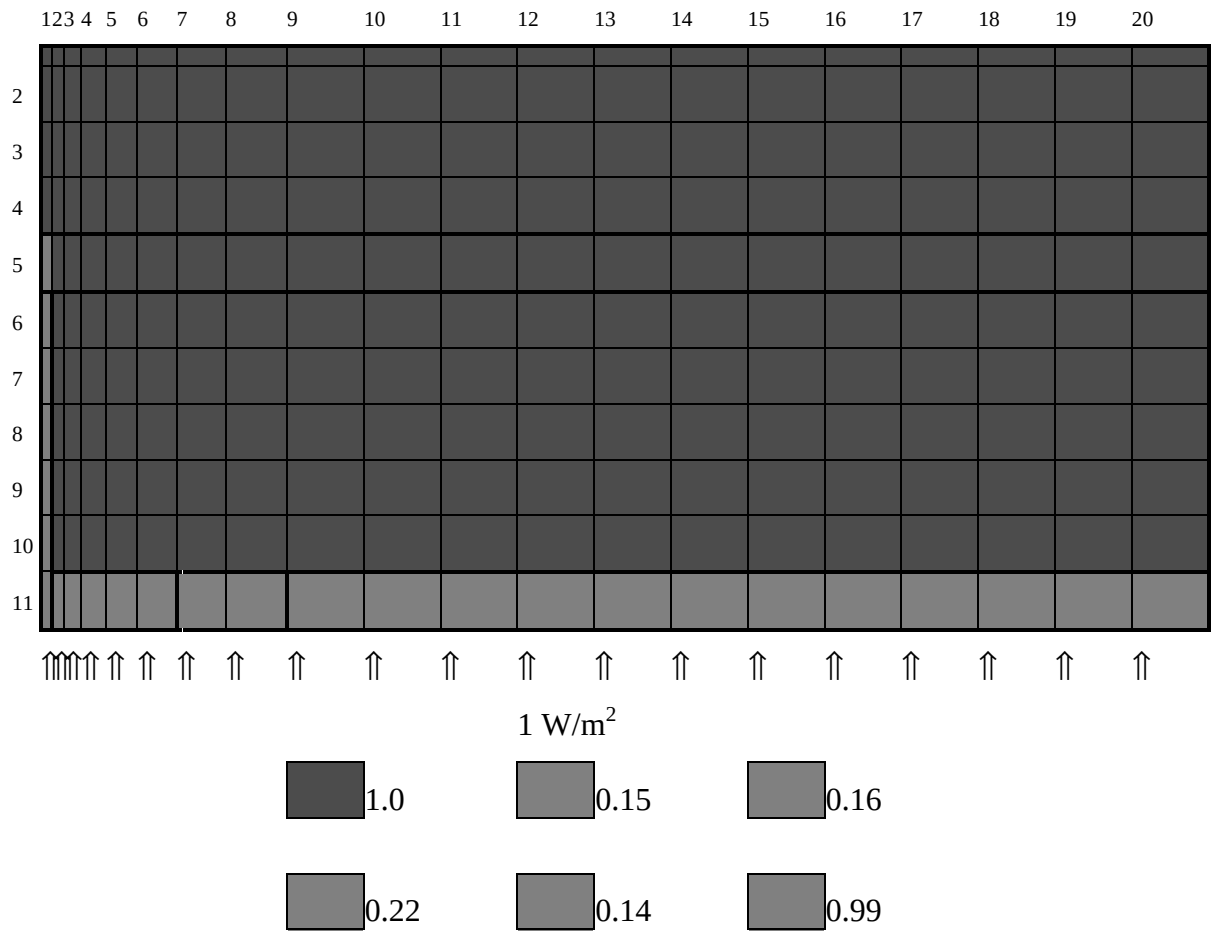

Figure 6.10: Liquid saturation distribution for Model V.

6.5 CONCLUSIONS

Capillary forces play an important role in determining the natural state of fractured geothermal reservoirs. Capillarity tends to keep the vapor phase in the fractures and the liquid phase in the matrix. In this manner, the fractures are not fully saturated with liquid and the possibility of having a heat pipe is increased. In Models III to V, the fractures were actually vapor-dominated heat pipes. A zero capillary pressure in the fracture blocks enhances the heat pipe effect, and also increases the transfer of liquid from the matrix into the fracture. Having low or no capillary pressure specified in the fracture blocks would improve the convection process and hence speed up heat transfer.

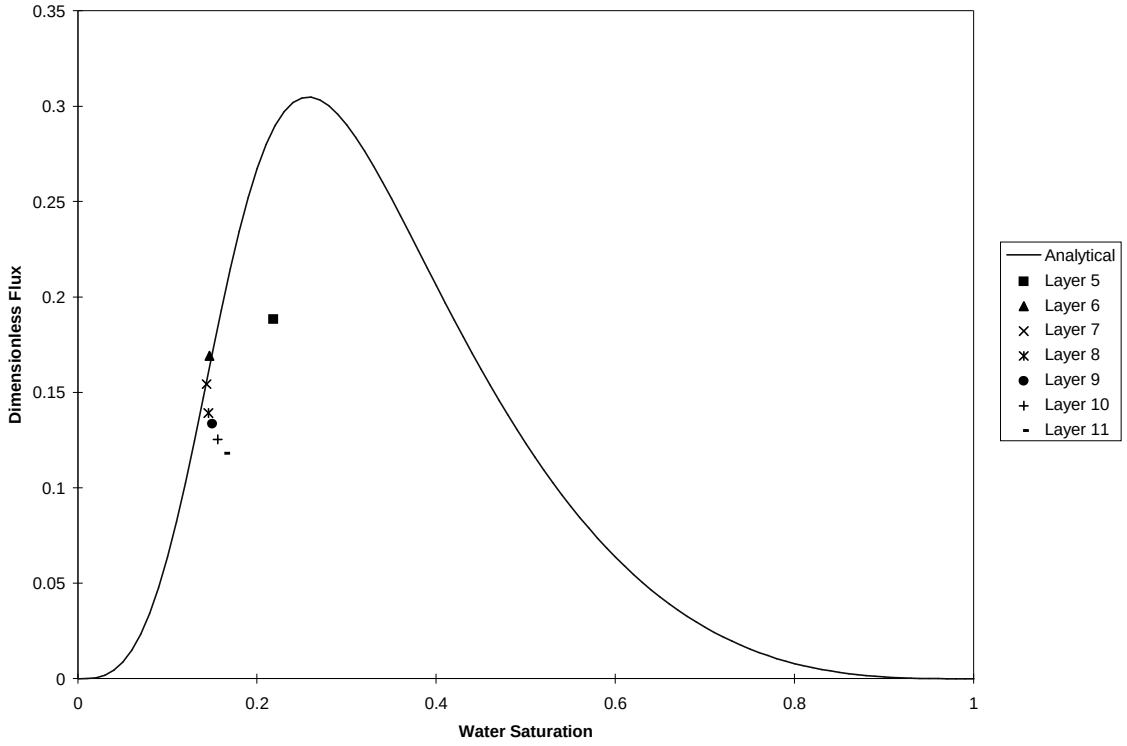

Figure 6.11: Plot of the dimensionless heat flux versus saturation for the fracture blocks of Model V.

Based on the results obtained from Model II, it seems that an appropriate value for capillary pressures in fractures would be less than 200 kPa. This is reasonable due to the inverse relationship capillary pressure has with the mean pore radius. Since the mean pore radius is "large," small capillary pressures are expected.

Capillary pressures are likewise important as far as the stability of a water-saturated region on top of a liquid-dominated two-phase zone is concerned. Having a zero matrix capillary pressure (Model I) will cause the two-phase zone to collapse under the water-saturated zone.

The two-dimensional fractured model demonstrates that due to capillary forces, a liquid-dominated two-phase zone will remain stable under a water-saturated region. Normally, one would think that due to the presence of a high permeability conduit, the liquid would gush through the fracture and quench the two-phase zone, however, this is not necessarily the case.

The numerical stability of this system suggests that it is not necessary to model a geothermal system as having a caprock on top. This is the same observation made by Sondergeld and Turcotte (1977) based on their experimental results.

7 MODELING OF GEOTHERMAL RESERVOIRS CONSTRAINED TO INJECTION RETURN DATA

This project is being conducted by Prof. Roland Horne and Graduate Research Assistant Ma. Michelle Sullera. It aims to deduce injection return mechanism(s) and flow paths from correlations between producer chloride concentration and injection operating parameters (flow rate and injection chloride).

7.1 BACKGROUND

Previously, production and injection data from Palinpinon-I geothermal field in the Philippines were analyzed using the following models:

Correlation 1

$$Cl_p = a_0 + a_1 Q_{I1} + a_2 Q_{I2} + a_3 Q_{I3} + \ldots \quad + a_n Q_{In} \tag{7.1}$$

Correlation 2

$$Cl_p = a_0 + a_1 Q_{I1} + a_2 Q_{I2} + a_3 Q_{I3} + \ldots \quad + a_n Q_{In} + bt \tag{7.2}$$

where Cl_p = chloride concentration in production well, *P*

Q_{In} = mass flow rate to injection well, I_n

a_n = linear coefficient of well I_n

a_0 = a constant associated with local chloride concentration

t = time

It was shown that Correlation 2 fits the data better than Correlation 1; however, Correlation 2 was also shown to have a poor 'predicting capacity.'

7.2 LATEST RESULTS AND DISCUSSION

Regression analysis similar to that previously applied to data from Dixie Valley was used to analyze Palinpinon data. Despite having been shown to have poor predicting capacity, Correlation 2 gave high values of regression coefficient (0.90 and higher).

Assuming that Correlation 2 more appropriately models the data, the data set was then subjected to the P-test using Microsoft Excel's regression analysis tool. According to this test, the dependent variable (in this case, the produced fluid chloride concentration) is (100-x)% certain to be related to independent variables (in this case, injection rates) which have P-values of x%. Setting the 'correlation limit' to P-values less than or equal to 5% that is, assuming that only injection wells with corresponding P-values less than 5% are certainly affecting the chloride concentration of a particular producer, new individual linear models were constructed for each of the producing wells. These linear models take into account the effect only of the correlatable injection wells which were deduced from the P-test. The new models had regression coefficients as high as the previous models (>0.90). A summary of the calculated coefficients is given in Table 7.1.

Table 7.1: Coefficients for the new 'limited' linear models.

PRODUCER	a_0	a_1	a_2	a_3	a_4	a_5	a_6	a_7	a_8	a_9	b
OK-7	5269.430	**5.207**	**-24.848**			**14.148**	**-4.452**			**9.582**	709.835
OK-9D	4190.073			**3.752**	**4.203**	**-11.137**				**2.648**	354.025
OK-10D	3690.433	**4.465**					**3.841**				99.946
PN-31D	4198.583								**4.289**	**8.733**	680.031
PN-30D	4430.963			**4.803**					**-3.159**		175.269
PN-29D	4772.351						**-4.729**			**5.658**	963.181
PN-28	5678.132						**-4.947**				719.563
PN-27D	3910.526				**0.922**					**8.076**	549.192
PN-26D	5910.738	**2.823**									730.807
PN-24D	3909.668								**3.466**		555.714
PN-23D	4393.005			**3.620**			**-1.941**		**-1.562**		487.299
PN-21D											
PN-20D											
PN-19D	5090.105			**-7.313**			**-5.160**		**4.558**		613.611
PN-18D	4704.682		**-19.587**								695.699
PN-17D	5172.044	**3.712**							**-4.190**		843.556
PN-16D	3839.213			**-4.448**					**2.365**		587.888
PN-15D	4741.449				**-5.233**						725.341
PN-14											

As shown in Table 7.1, even the new linear models have some negative coefficients.

As a first test of the applicability of these linear models, conclusions deduced from these models were compared to the results of actual tracer tests conducted on injector 9 (I_9) (corresponding to coefficient a_9 in Table 7.1.) These tracer test results are listed in Table 7.2.

Table 7.2: Tracer test results

	Tracer Test on I_9
	AFFECTED WELLS
MOST AFFECTED	OK-7
	PN-26D
	PN-28
	PN-29D
	PN-18D
	PN-23D
	PN-16D
LEAST AFFECTED	PN-19D

According to the linear models, a significant portion of the injection returns to producers OK-7, OK-9D, PN-31D, PN-29D, and PN-27D come from injector I_9 and thus we may expect some kind of connection between these producers and I_9. The proposed connection between OK-7, PN-31D, and PN-29D and I_9 were confirmed by the tracer test results, but not the deduced connection of I_9 to wells OK-9D and PN-27D.

The preceding observations however, do not necessarily nullify the linear models. The linear models deduce the contribution of different injection wells to a particular producer, whereas the tracer test tells us the distribution of injected fluids from a particular injector into different producers. These are two different things. The fact that producer A gets most of its injection returns from injector B does not necessarily imply that most of what is injected to injector B would go to producer A. It would be more appropriate, it seems, to compare tracer test results with predictions from linear models which relate injection rate to production chloride concentrations. Realistically speaking, however, injection rate is not a dependent variable, nor are production chloride concentrations controllable variables.

Therefore the most we could get from comparing model predictions with tracer test results was a qualitative confirmation or denial of connections between producers and injectors.

7.3 CONTINUING WORK

Similar analysis will be applied to Dixie Valley data, and connections between producers and injectors established from this analysis would be further tested by incorporating them into a numerical model and generating production history matches.

8. REFERENCES

Akin, S., Demiral, B., and Okandan, E., (1996): "A Novel Method of Porosity Measurement Utilizing Computer Tomography", *In Situ*, **20**(4), 347-365

Ambusso W. J., (1976), "Experimental Determination of Steam-Water Relative Permeability Relations," MS Report, Stanford University, Stanford, California.

Bau, H. M. and Torrance, K. E. (1982). Boiling in low-permeability porous materials. *Int. J. of Heat Mass Transfer* **25**, 45-55.

Bodvarsson, G. (1969). On the temperature of water flowing through fractures. *J. Geophys. Res.* 74(8), 1987-1992.

Bodvarsson, G. (1972). Thermal problems in the siting of reinjection wells. *Geothermics* **2**(1), 63-66.

Cengel, Y. A., and Boles, M. A., (1989), "Thermodynamics, An Engineering Approach," McGraw-Hill, New York, New York.

Chawathe, A., and Sharma, M. P., (1991), "Effects of Temperature on the Permeability of Porous Media," Multiphase Transport in Porous Media, ASME, FED-Vol. 122/HTD-Vol. 186.

Drummond, J. E. and McNabb, A. (1972). The heating of cold-water intrusions in a geothermal field. *N. Z. J. Sci.* **15**(4), 665-672.

Eastman, G. Y. (1968): The heat pipe. *Sci. American* **218**, 38-64.

Grant, M. A. and Studt, F. E. (1981). A conceptual model of the Tongonan geothermal reservoir. *Pap. GEOSEA Conf. 4th, 1981.*

Grindley, G. W. (1965). Wairakei. *New Zealand Volcanology*. 157.

Hornbrook, J. W. and Faulder, D. D. (1993). Parametric analysis of factors affecting injection and production in geothermal reservoirs. *Proc. Stanford Geoth. Workshop* **18**, 53-60.

Johns, R. A., Steude, J. S., Castanier, L. M., and Roberts, P. V., (1993), "Nondestructive Measurements of Fracture Aperture in Crystalline Rock Core Using X-Ray Computed Tomography," J. Geophys, Res., 98 (B2), pp. 1889-1900.

Nathenson, M. (1975). Physical factors determining the fraction of stored energy recoverable from hydrothermal convection systems and conduction dominated areas. *Geol. Surv. Open-File Rep.* (U.S.) 75-525.

Piquemal, J., (1994), "Saturated Steam Relative Permeabilities of Unconsolidated Porous Media," Transport in Porous Media 17, pp. 105-120.

Pruess, K. (1985). A quantitative model of vapor dominated geothermal reservoirs as heat pipes in fractured porous rock. *Geothermal Resources Council: Transactions* 9(II), 353-361.

Pruess, K. (1991). Grid orientation and capillary pressure effects on the simulation of water injection into depleted vapor zones. *Geothermics* **20**(No.5/6), 257-277.

Satik, C., Ambusso, W., Castanier, L. M., and Horne, R. N., (1995), "A Preliminary Study of Relative Permeability in Geothermal Rocks," GRC Transactions, Vol. 19, pp. 539-543, October.

Satik, C., (1994), "Studies in Vapor-Liquid Flow in Porous Media", *Ph.D. Thesis*, University of Southern California, Los Angeles, CA

Satik, C., (1997), "Experiments of Boiling in Porous Media", Proc. of 22nd Stanford Workshop on Geothermal Reservoir Engineering, Stanford, CA

Satik, C. and Yortsos, Y.C., (1996), "A Pore Network Study of Bubble Growth in Porous Media Driven by Heat Transfer", *J. Heat Transfer,* **118**

Sondergeld, C. H. and Turcotte, D. L. (1977). An experimental study of two-phase convection in porous medium with applications to geological problems. *J. Geophys. Res.* **82**(14), 2045-2053.

Trimble, A. E., and Menzie, D. E., (1975), "Steam Mobility in Porous Media," Paper SPE 5571 presented at the 50th Annual Fall Meeting, SPE of AIME, Dallas, Texas, September.

White, D. E. L., Muffler, J. P. and Truesdell, A. H. (1971). Vapor-dominated hydrothermal systems compared with hot-water systems. *Econ. Geol.* **66**,75-97.